Protected Convection as a Metric of Dry Air Influence on Precipitation

FIAZ AHMED[a] AND J. DAVID NEELIN[a]

[a] *Atmospheric and Oceanic Sciences, University of California, Los Angeles, Los Angeles, California*

(Manuscript received 26 May 2020, in final form 24 January 2021)

ABSTRACT: Entrainment of dry tropospheric air can dilute cloud buoyancies and strongly affect the occurrence and intensity of convection. To measure this dry air influence on tropical precipitation, rainfall values that would occur when convection is "protected" from dry air dilution are estimated. An empirical relationship between tropical oceanic precipitation and entraining buoyancy in the lower troposphere (from the surface to 600 hPa) is leveraged. Protected buoyancies are computed by allowing a plume model to entrain saturated air at environmental temperature. These buoyancies are then used to estimate precipitation from protected convection. In most regions, the protected precipitation greatly exceeds the observed precipitation. Warm waters adjoining continents display striking disparities between observed and protected rainfall pointing to rainfall climatologies severely limited by dry air. The most prominent of these regions include the Red Sea and the Persian Gulf, followed by the Caribbean Sea, the Gulf of Mexico, and the seas surrounding the Maritime Continent. We test if similar large precipitation values are realizable in the Community Atmospheric Model (CAM5), wherein the parameterized convection in small ($\sim 2^\circ \times 2^\circ$) pockets is allowed to only entrain saturated air. The precipitation within these pockets shows strong enhancement that is maintained over time, and is compensated by slight reductions in neighboring regions. In the model, protecting convection yields larger precipitation values over ocean than over land; protected precipitation also intensifies in a uniform SST warming experiment. The model experiments suggest that protected pockets in numerical simulations could be used to mimic the consequences of meteorological protection—from closed circulation or moisture shielding effects—that generate extreme precipitation.

KEYWORDS: Atmosphere; Tropics; Buoyancy; Entrainment; Precipitation

1. Introduction

It is well known that dry air impacts tropical rainfall. Early researchers recognized that cloudy air properties are diluted upon mixing with environmental air (Stommel 1947; Austin 1948; Warner 1955). They also deduced that the mixing process is a consequence of entrainment due to vertical acceleration in deep convective clouds (Houghton and Cramer 1951). In the tropics, the dilution of cloud properties is known to be pervasive enough (Zipser 2003; Fierro et al. 2009; Romps and Kuang 2010) to regulate the occurrence and depth of moist convection (Brown and Zhang 1997; Sherwood 1999; Jensen and Del Genio 2006; Holloway and Neelin 2009; Schiro et al. 2016).

When cloudy elements are protected from dry air dilution, the result appears to be a concomitant increase in precipitation intensity. For instance, high-resolution modeling studies have shown that moist protective shells (Dawe and Austin 2011; Yeo and Romps 2013; Hannah 2017; Becker et al. 2018) around tropical convective elements arrest dilution. As a result, aggregated convective elements are hypothesized to benefit from greater mutual protection (Feng et al. 2015; Moser and Lasher-Trapp 2018) that can prolong lifetimes and increase precipitation rates. A similar mechanism may allow tropical coastal precipitation to occur in relatively dry environments (Bergemann and Jakob 2016). Closed circulations in critical layers of easterly waves are hypothesized to limit dilution and support the growth of pretropical storm disturbances (Dunkerton et al. 2009; Montgomery et al. 2010; Wang et al. 2010). The inner core of developed tropical cyclones (TCs) is also shielded by "moist envelopes" (Braun et al. 2012; Kimball 2006; Fritz and Wang 2013) that emerge as a consequence of the inertial stability (Schubert and Hack 1982; Willoughby et al. 1984) limiting radial inflow above the boundary layer. Thermodynamic properties that are consistent with the lack of dilution have also been observed in severe midlatitude storms (Davies-Jones 1974; Bluestein et al. 1988; Bryan et al. 2003).

The geographical distribution of precipitation that would result from the absence of dry air dilution—or "protected" precipitation—is a key target of this study. This distribution will be used highlight regions whose precipitation climatology is most limited by dry air. To construct the protected precipitation climatology, we require an estimator of area-averaged precipitation for the tropics that also contains an explicit dependence on dry air dilution. A recently documented empirical relationship (Ahmed and Neelin 2018, hereafter AN18; Schiro et al. 2018, hereafter S18; Ahmed et al. 2020) between area-averaged tropical precipitation and a measure of buoyancy in the lower troposphere (B_L) proves adequate for this purpose. The B_L variable condenses environmental moisture and temperature information through the buoyancy of a bulk, entraining plume (Betts 1975; Jakob and Siebesma 2003; Holloway and Neelin 2009). The B_L variable measures the environmental support for convection and does not directly correspond to the buoyancy of convecting entities. Every B_L value is associated with an area-averaged precipitation expected value; the precipitation increases with B_L above a threshold value in a relationship that holds robustly across tropical oceans. This precipitation–B_L relationship explains geographical variations noted in other empirical relationships, including those between tropical precipitation and column-integrated moisture and temperature

Corresponding author: Fiaz Ahmed, fiaz@ucla.edu

DOI: 10.1175/JCLI-D-20-0384.1

variables (Bretherton et al. 2004; Peters and Neelin 2006; Neelin et al. 2009; Ahmed and Schumacher 2015; Kuo et al. 2018; Rushley et al. 2018). Prior results using column-integrated moisture (Ahmed and Schumacher 2015, 2017) suggest that area-averaged precipitation changes with B_L are primarily due to changes in the areal coverage of precipitation. This is consistent with radar-based studies that report a strong link between area-averaged precipitation and the precipitating area fraction (Davies et al. 2013; Kumar et al. 2015; Louf et al. 2019; Powell 2019). There are likely other such finer-scale details that underpin the physics of the precipitation–B_L relationship; for example, the cloud microphysics, the measurement of entrainment (Romps 2010; Yeo and Romps 2013), the fundamental structure of convecting entities (Sherwood et al. 2013; Romps and Charn 2015; Morrison et al. 2020), and their true local buoyancies. In this study, we sidestep these considerations and instead leverage the robustness of the precipitation–B_L relationship to directly estimate protected precipitation.

The buoyancy measure B_L combines information about (i) the boundary layer moist static energy (or equivalent potential temperature) relative to the free tropospheric temperature, akin to convective available potential energy (CAPE), and (ii) the lower-free-tropospheric saturation level. The B_L measure can be partitioned to separately account for contributions from a saturated component ($B_{L\text{-sat}}$) and effects of dilution ($B_{L\text{-sub}}$). Specifically $B_{L\text{-sat}}$ provides an estimator of the precipitation that potentially could occur when the entrained environmental air is saturated at environmental temperature—with the further assumption that other factors affecting precipitation remain constant. The latter caveat is more likely satisfied over the tropical oceans, where the large-scale balances enforce relatively invariant boundary layer properties (Emanuel 1995; Raymond 1995; Emanuel 2019) and free tropospheric temperature profiles (Sobel and Bretherton 2000; Sobel et al. 2001). Our analysis will therefore primarily focus on ocean regions. In the first part of the study, we create a climatology of protected precipitation using $B_{L\text{-sat}}$. In the second part of this study, we use version 5 of the Community Atmospheric Model (CAM5) to test the consequences of protecting parameterized convection in the model. A brief description of the reanalysis data and modeling tools is provided in section 2. Section 3 outlines the method used to create the empirical protected precipitation product from reanalysis information. Section 4 highlights noteworthy dry air limited regions of the tropical and subtropical oceans using the protected precipitation product. Section 5 reports the preliminary consequences of artificially enforcing protection of convection in CAM5. In section 6, additional experiments probe the sensitivity of parameterized CAM5 convection to the details of protection and to uniform surface warming. Section 7 contains a summary and discussion of our main results.

2. Data, models, and methods

a. Reanalysis data

We use profiles of temperature and specific humidity on pressure levels from the ERA5 reanalysis (Hersbach et al. 2020) sampled every 3 h on a 0.25° horizontal grid. The ERA5 information was regridded to match the 0.25° gridded, 3-hourly precipitation data from the Tropical Rainfall Measuring Mission (TRMM 3B42; Huffman et al. 2007). The thermodynamic and precipitation data were used for a 13-yr period spanning from 2002 to 2014.

b. Entraining plume model

We use an entraining plume model to compute the empirical buoyancy measure B_L. The plume is initialized near the surface, and conserves the ice–liquid water potential temperature (θ_{eil}; Emanuel 1994) during phase change. Plume liquid water content exceeding 1 g kg^{-1} is assumed to rain out. The plume is assumed to mix environmental air in accordance with the deep-inflow mixing profile (Holloway and Neelin 2009; Schiro et al. 2016; S18). In this mixing profile, the plume incorporates nearly the same mass of environmental air at every level between the surface and the freezing layer. The assumptions of the deep-inflow mixing formulation are consistent with observed reports of vertically deep lateral inflow into strong tropical convection (Ferrier and Houze 1989; Kingsmill and Houze 1999; Mechem et al. 2002). Upon translating the mixing profile to fractional mixing coefficients (expressed in km^{-1}), the obtained coefficients are inversely proportional to altitude [see "Deep inflow B" in Holloway and Neelin (2009) and Schiro et al. (2016)]. The plume computation then yields the plume virtual temperature, which is used to define B_L:

$$B_L = \frac{1}{(p_s - p_L)} \int_{p_L}^{p_s} g \left(\frac{T_{vp} - T_v}{T_v} \right) dp, \tag{1}$$

where T_{vp} and T_v are the virtual temperatures of the plume and the environment, respectively; g is a constant acceleration due to gravity (9.8 m s^{-2}), and p_s is the surface pressure. We use p_L = 600 hPa, since an average over the lower troposphere is adequate to construct the precipitation statistics. The measure of B_L in (1) is a close numerical analog to the analytic version used in AN18, in which B_L is a function of *layer-averaged* equivalent potential temperature θ_e. In contrast, the function in (1) uses the full vertical structure of ERA5 temperature and moisture in the lower troposphere, and therefore includes effects of any sharp vertical gradients. This sensitivity allows B_L computed using (1) to better discern features such as local temperature inversions. Protected buoyancies are computed by allowing the plume model to only entrain saturated air at the environmental temperature; the entrainment associated with both turbulent and coherent inflow to convective plumes may still be present. Allowing the plume to entrain saturated air nearly renders the plume undilute since differences between plume and environmental sensible heat values are negligible (Waite and Khouider 2010). Hereon, we will use the terms "protected" and "undilute" interchangeably to refer to plume-specific quantities computed by entraining saturated air.

To examine the relative importance of protection in different vertical layers, we also consider "partially protected" buoyancies. These are computed by allowing the plume model to entrain saturated air in the bottommost 200-hPa layer

TABLE 1. Summary of the different model runs used in this study.

Experiment	Run length (years)	Description
CTRL	3	Control run with observed SSTs, initialized on 1 Jan 1979.
PROT	3	As in CTRL, but with the modified ZM scheme. In selected locations, saturated air is entrained in DCAPE closure, and by updrafts and downdrafts. No re-evaporation.
ENTOFF	2	As in CTRL, but with no entrainment in DCAPE closure.
C0EXP	2	As in PROT, but precipitation efficiency (C_0) same over land and ocean.
CLIM (PROT and CTRL)	2	As in PROT and CTRL, but with climatological SSTs.
CLIM2K (PROT and CTRL)	2	As in CLIM, but with uniform 2-K SST increment.

(~1000–800 hPa over tropical oceans), and observed unsaturated environmental air through the rest of the lower troposphere (~800–600 hPa). The dilute, fully protected, and partially protected versions of the plume model are run over all tropical ocean points on the ERA5 grid between 35°N and 35°S for a 13-yr time period between 2002 and 2014.

c. *Community Atmospheric Model experiments*

The CAM5 model (Neale et al. 2012) at a horizontal resolution of 0.9° latitude × 1.25° longitude is used to test the implications of our empirical predictions. This model is equipped with the Zhang–McFarlane (ZM) cumulus parameterization scheme (Zhang and McFarlane 1995) that characterizes subgrid-scale convection using the properties of a bulk plume. The closure in the ZM scheme consumes dilute CAPE (DCAPE; Neale et al. 2008). Protection from dilution is enforced within small specified regions such that the parameterized convection only mixes with saturated environmental air. In the ZM scheme, the mixing between the plume and the environmental air is specified in two different locations. The first of these locations is the convective closure, in the FORTRAN subroutine *closure*. In the second location—within the FORTRAN subroutine *cldprp*—a spectrum of convective updrafts and downdrafts also mix in environmental air at different entrainment rates than the prescribed value in the closure. The launch level for the model convection is still determined by the nonprotected environmental properties—which in the ZM scheme is governed by the level of maximum moist static energy. The different model experiments used are detailed below; these experiments vary in the type of protection enforced, parameter values, and surface boundary conditions.

1) STANDARD PROTECTED AND CONTROL RUNS

The CAM5 model is initialized on 1 January 1979 with observed sea surface temperatures (SSTs) and is allowed three months of spinup. A 3-yr control run (CTRL) is subsequently produced. Protection is enforced in the standard protected run (PROT) by (i) computing DCAPE with saturated environmental air in the subroutine *closure*, (ii) ensuring that the convective updrafts and downdrafts only mix saturated environmental air in the subroutine *cldprp*, and (iii) suppressing the re-evaporation of convective rain within the subroutine *zm_conv_evap*. These modifications to the ZM scheme are consistent with the physical assumption that the air being entrained is saturated. The PROT run is generated for the same 3-yr period as CTRL.

2) TWO VARIANTS OF STANDARD PROTECTION

Two additional variants of the PROT run are also generated. In the first variant, termed ENTOFF, only the closure is modified by setting entrainment to zero in the DCAPE computation. In contrast to the PROT run, the spectrum of updrafts and downdrafts in ENTOFF still interact with the environmental unsaturated air, and re-evaporation of rainwater is present. The protection from unsaturated air is therefore weaker in ENTOFF than in PROT. The ENTOFF run is produced for two years and is used to test the sensitivity of CAM5 convection to changes in the degree of protection.

Within the ZM scheme, the precipitation efficiency coefficient in the ZM scheme (C_0) controls the fraction of the cloud water flux that is converted to rainwater [see Eq. (7) in Zhang and McFarlane 1995]. In the standard version of CAM5, this coefficient takes different values over land ($C_0 = 0.0059\,\mathrm{m}^{-1}$) and ocean ($C_0 = 0.045\,\mathrm{m}^{-1}$). A second variant of the standard protected run is generated by retaining same modifications to the ZM scheme as in PROT, but changing C_0 to have the same value over both land and ocean ($C_0 = 0.045\,\mathrm{m}^{-1}$). This run is hereafter termed C0EXP, and is used to investigate certain land–ocean differences in protected precipitation magnitudes. The C0EXP run like ENTOFF is produced for two years.

3) FIXED SST RUNS

To investigate how the properties of protected convection vary with climate, two sets of experiments with fixed SSTs—similar to Cess et al. (1990) and Cess et al. (1996)—were performed. First, a pair of 2-yr runs—with and without protection—termed CLIM runs are generated with present-day climatological SSTs. These CLIM runs are equivalent to CTRL and PROT in all aspects apart from the SST forcing. A second pair of 2-yr control and protected runs termed CLIM2K runs are produced with an SST field that is uniformly warmer by 2 K.

Table 1 summarizes the model experiments used, and details the changes to the ZM scheme and the SST field. The modified ZM codes are publicly available at the web address provided in the acknowledgments section. The DCAPE values are computed online within the ZM scheme in the FORTRAN subroutine *buoyan_dilute*. The protected version of DCAPE is simply termed CAPE, and is computed by entraining saturated

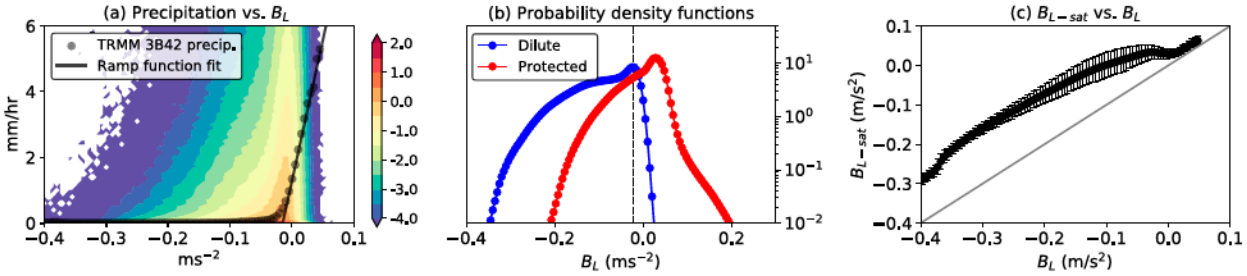

FIG. 1. (a) Conditionally averaged precipitation as a function of B_L (black scatter) and the ramp function fit (solid black line). The width of each bin on the x axis is 0.005 m s^{-2}, and only bins containing a minimum of 100 samples are shown. The joint pdf of B_L and precipitation is shown in colored contours; the accompanying color bar shows the $\log_{10}$ of the joint pdf. (b) The probability density functions of the protected (red) and dilute B_L values (blue). (c) Protected B_L conditionally averaged as a function of the dilute B_L; the one-to-one line is in gray, and the error bars denote the standard error in each bin.

environmental air within the same subroutine. We output daily averaged values of total precipitation, DCAPE, and CAPE.

3. An empirical precipitation estimator

We now explore how B_L can be employed as a statistical *predictor* of precipitation. We use the predictor to ask what the precipitation would be if the entrained environmental air were saturated, assuming that the temperature in the environment remains approximately unchanged. The temperature variability is smaller over tropical oceans due to strong constraints on the boundary layer thermodynamic properties (Emanuel 1995; Raymond 1995; Emanuel 2019) and the free-tropospheric gravity wave response (Sobel and Bretherton 2000; Sobel et al. 2001). Over land, however, the boundary layer thermodynamic properties are more variable due to the diurnal cycle of solar radiation and soil moisture feedbacks (Eltahir 1998; Cook et al. 2006; Hohenegger et al. 2009). We therefore restrict our analysis of protected precipitation in empirical estimates to the tropical ocean regions. We comment on protected convection over tropical land using results from CAM5 in sections 5 and 6.

The black dots in Fig. 1a show the tropical oceanic precipitation from the 3-hourly, 0.25° TRMM 3B42 dataset conditionally averaged by spatiotemporally matched B_L values. Here, B_L is computed using the entraining plume model run for a single year (2014), since this supplies sufficient samples to construct robust precipitation statistics. The sharp pickup in conditionally averaged precipitation, $\langle P \rangle$ is captured by the ramp function:

$$\langle P \rangle = \alpha(B_L - B_c)H(B_L - B_c). \tag{2}$$

Here, H is the Heaviside function. The parameters α and B_c are estimated using a linear fit for $\langle P \rangle$ values between 0.5 and 4 mm h^{-1}, which yields the slope $\alpha \approx 86$ mm h^{-2} (m s^{-2})$^{-1}$ and the x-intercept $B_c = -0.01$ m s^{-2}. These parameters are invariant to changes in the time period of analysis and, to some extent, in the horizontal resolution of the dataset used (not shown). The joint probability density function (pdf) between precipitation and B_L is also shown in Fig. 1a. For a given value of B_L, a vast majority of samples are weakly precipitating or nonprecipitating, and occupy the smallest precipitation bin (<0.1 mm h^{-1}); the occurrence probabilities for higher precipitation values drop, albeit more slowly than a Gaussian distribution. As B_L increases beyond B_c, the relative fraction of nonprecipitating points reduces, leading to increases in the conditional mean precipitation. This dependence of the conditional precipitation distribution on B_L is similar to the dependence on column water vapor (Kuo et al. 2018).

While the formulation of B_L may appear similar to DCAPE (Neale et al. 2008; Molinari et al. 2012; Singh and O'Gorman 2013), three key differences are emphasized. First, the levels of integration in a traditional CAPE calculation only span positive buoyancy values, whereas B_L includes both positive and negative values, and is therefore impacted by convective inhibition. Second, in contrast to most CAPE computations with a constant mixing assumption (e.g., Neale et al. 2008; Molinari et al. 2012), the mixing coefficients in the B_L computation vary as z^{-1}, where z is the height above surface. Third, the relationship between precipitation and DCAPE with constant mixing (Schiro and Neelin 2019) tends to be weaker than the precipitation–B_L relationship (especially if the mixing is not large).

It must also be recognized that the B_L measure that is strongly related to precipitation is nonunique. A family of related B_L measures similar to (1) can be generated by altering the parametric choices (e.g., the layer depth of integration, the plume conserved variable, virtual temperature/condensate effects, etc.). These variations do alter the fitting parameters α and B_c, but do not impact the linearity of the precipitating regime or the robustness of the relationship over tropical oceans, which we leverage to construct the protected precipitation dataset.

The undilute version of B_L, in which the plume only mixes in saturated environmental air, is termed $B_{L\text{-sat}}$. Figure 1b compares pdfs of B_L and $B_{L\text{-sat}}$ and shows that the leading-order effect of protection is a rightward translation of the B_L pdf. More detailed differences lie in the tails of the distribution; B_L has a sharp drop-off in occurrence beyond B_c, while the right tail of $B_{L\text{-sat}}$ drops more slowly than B_L. The differences between these pdfs, together with the precipitation–B_L relationship in Fig. 1a, imply large precipitation values when protection from dilution is enforced. Figure 1c shows $B_{L\text{-sat}}$ conditionally averaged (or binned) by co-occurring B_L values.

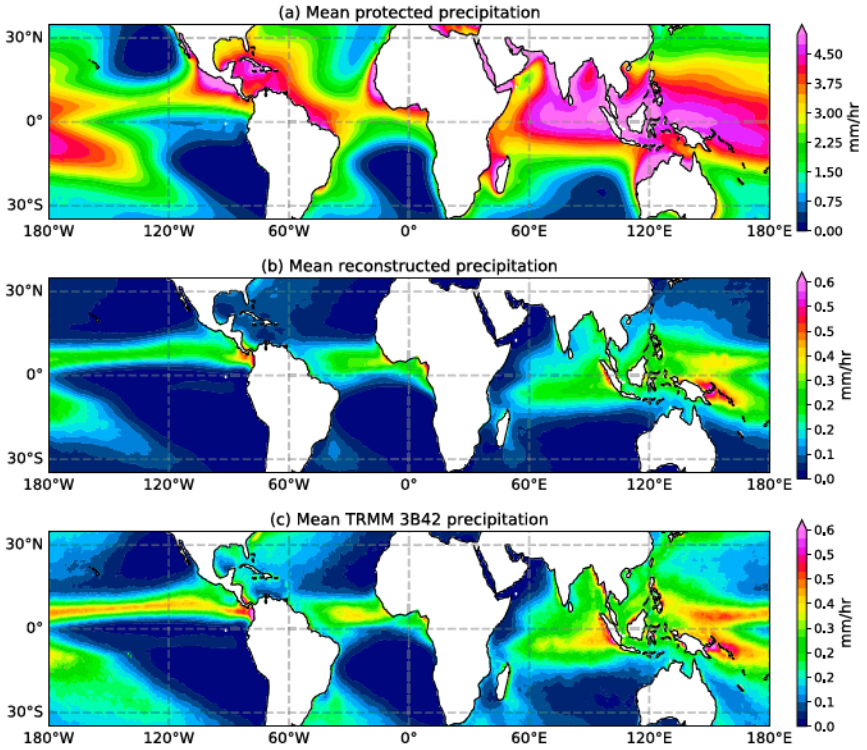

FIG. 2. (a) Protected precipitation, (b) reconstructed mean precipitation, and (c) TRMM 3B42 precipitation averaged between 2002 and 2014. The color bar range in (a) is different from the range in (b) and (c). Protected and reconstructed mean precipitation are computed using (2) along with ERA5 temperature and moisture values. See text for details.

We see that when $B_L < B_c$, $B_{L\text{-sat}}$ always exceeds B_L—indicating that dry air has a significant influence on plume buoyancies below the critical value for precipitation onset. For values of $B_L > B_c$, both B_L and $B_{L\text{-sat}}$ converge toward the one-to-one line, suggesting that B_L values farther above the precipitation onset are more likely to be protected, possibly due to a near-saturated lower troposphere. However, the pdf of B_L suggests that such instances are relatively rare.

While the actual precipitation field is noisy, the moments of precipitation are somewhat more amenable to prediction (Raymond and Flores 2016). Our target field is a long-term (seasonal and beyond) mean of precipitation deduced solely from B_L using (2). There are two sources of noise contained within the relationship in (2): (i) variations in precipitation for a given value of B_L, and (ii) stochastic fluctuations in the value of B_c. The first source of noise generates a precipitation distribution for each value of B_L, as seen from the joint pdf in Fig. 1a. The second source of noise contributes to the curvature in the conditionally averaged precipitation curve near B_c (e.g., Stechmann and Neelin 2011; Ahmed et al. 2020). This source accounts for factors besides B_L (e.g., the microphysics) that impact precipitation. The relationship in (2) incorporates the first source of noise, so variations in precipitation for a given value of B_L do not greatly affect the precipitation estimate. The estimator is expected to fare less well if there are strong stochastic fluctuations in the value of B_c.

4. Empirical protected precipitation

The $B_{L\text{-sat}}$ value for each tropical ocean grid point from ERA5 and the analytic fit in (2) are used to construct an 8 times daily protected precipitation field for the 13-yr period from 2002–14. An estimate of the observed precipitation field is also constructed using the B_L value instead of $B_{L\text{-sat}}$ for each grid point to check how well the TRMM 3B42 precipitation is reconstructed when observed moisture is entrained. Figures 2a and 2b show the protected and reconstructed precipitation fields respectively, averaged over the 13-yr time period, alongside the corresponding mean TRMM 3B42 precipitation in Fig. 2c. From Fig. 2a it is clear that protection from dry air generally results in stronger precipitation. The precipitation enhancement from protection is generally greater over warmer waters, and varies from up to a factor of 2 in tropical convergence zones to several orders of magnitude over the subtropical waters. Even though the measure of potential precipitation from protection is displayed as a continuous map in Fig. 2a, we assume that only a small region (or limited number of well-separated small regions) could reach these large precipitation values at a given time. That the enhancement of mean precipitation under protection results from increases in both persistence and intensity of precipitation can be inferred from the pdfs in Fig. 1. Locations with strong trade wind inversions in the Pacific and Atlantic Oceans show weak-to-nonexistent protected precipitation values. Even in a saturated

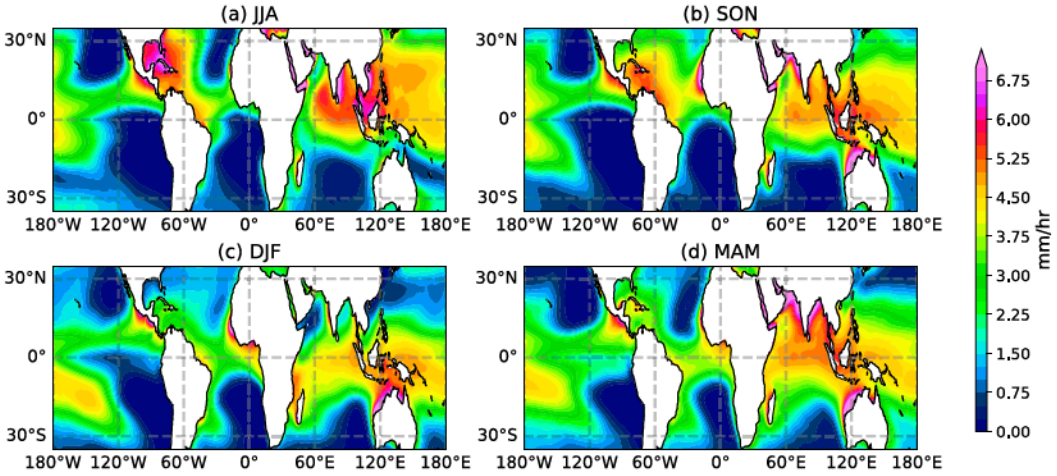

FIG. 3. Seasonally averaged protected precipitation for four different 3-month periods.

environment, the $B_{L\text{-sat}}$ values in these locations generally fall short of B_c, pointing to the role of temperature inversions in limiting precipitation from convection.

The reconstructed precipitation field in Fig. 2b calibrates the fidelity of the estimator in (2). The broad features of the observed mean tropical precipitation field (Fig. 2c)—including the warm pool, intertropical convergence zone (ITCZ), and the weakly precipitating subtropics—are well captured by the ramp function estimator. The precipitating zones in the reconstructed precipitation field are slightly less intense than in observation, as exemplified by an underestimation over the ITCZ region. The precipitation averaged over the tropical oceans in Figs. 2b and 2c is ~0.08 and ~0.13 mm h^{-1} respectively, so that the estimator in (2) has a bias of ~36%. With this calibration, we interpret the estimated protected precipitation field in Fig. 3a as a lower bound on the true annual mean precipitation that could result from protection. The statistical estimator in Fig. 1a was produced from only a single year (2014), yet shows out-of-sample skill in estimating the precipitation averaged across 14 years. This skill further highlights that the $\langle P \rangle - B_L$ relationship is not significantly impacted by year-to-year variations.

a. A metric for dry air influence

Seasonal variations in protected precipitation values are presented in Fig. 3. The averaging time period in this figure is separated by seasons: June–August (JJA), September–November (SON), December–February (DJF), and March–May (MAM). The values in Fig. 3 are interpreted as the potential precipitation that could occur if environmental moisture were replaced by its saturated value separately at each location. In Fig. 3, large protected precipitation amounts (>5 mm h^{-1}) are mostly found over warm waters adjoining land. In the boreal summer (Fig. 3a), these regions include the Caribbean Sea, the Gulf of Mexico, the Red Sea, the Persian Gulf, the South China Sea, and the shallow seas between Borneo and Sumatra. Waters to the northwest of Australia and also waters west of Mexico show prominent local maxima during SON and MAM (Figs. 3b,c), as do waters off the west African coast in SON (Fig. 3b). In all of these regions, the lower tropospheric temperature structure—mostly but not entirely due to a warm surface—supports $B_{L\text{-sat}}$ values that consistently exceed B_c. The warm tropical oceans also show substantial amounts of protected precipitation. However, excepting the Indian Ocean in JJA (Fig. 3a), these values are smaller ($\lesssim$4.5 mm h^{-1}) than those discussed for warm waters adjoining land. Conversely, the regions over the cold oceans under the descent regions of the subtropical highs have near-zero protected precipitation. In these regions, protecting convection is insufficient to generate large precipitation amounts, suggesting that convection is limited by factors other than dry air (i.e., a stable temperature profile, commonly including the effects of temperature inversions).

The large protected precipitation values highlighted in Fig. 3 are not realized in practice due to dilution by dry ambient air. In Fig. 4, we measure the influence of dry air in limiting precipitation by examining the protected precipitation values normalized by observed precipitation at every location. Regions with greater values of normalized protected precipitation are interpreted as being more limited by dry air. This dry air influence metric (Fig. 4) when interpreted alongside magnitudes of protected precipitation (Fig. 3) highlights four sets of regions:

1) *Large protected precipitation and small climatological precipitation.* These regions display large values of precipitation in the absence of dry air dilution (>6 mm h^{-1} in Fig. 3), but are close to nonprecipitating in the mean ($>10^2$ in Fig. 4), and mostly include warm waters adjoining arid landmasses. The lower tropospheric temperature structure supports convection, but the dryness of ambient air is a significant limiting factor. In regions such as the Red Sea, the Persian Gulf, and the Gulfs of Aden and Oman, a combination of a warm surface (Chaidez et al. 2017; Noori et al. 2019) and low climatological precipitation (Almazroui 2011; Almazroui et al. 2012) is particularly noteworthy. These regions are exceptionally dry air limited: protecting convection yields precipitation values that are nearly three orders of magnitude greater than the background precipitation.

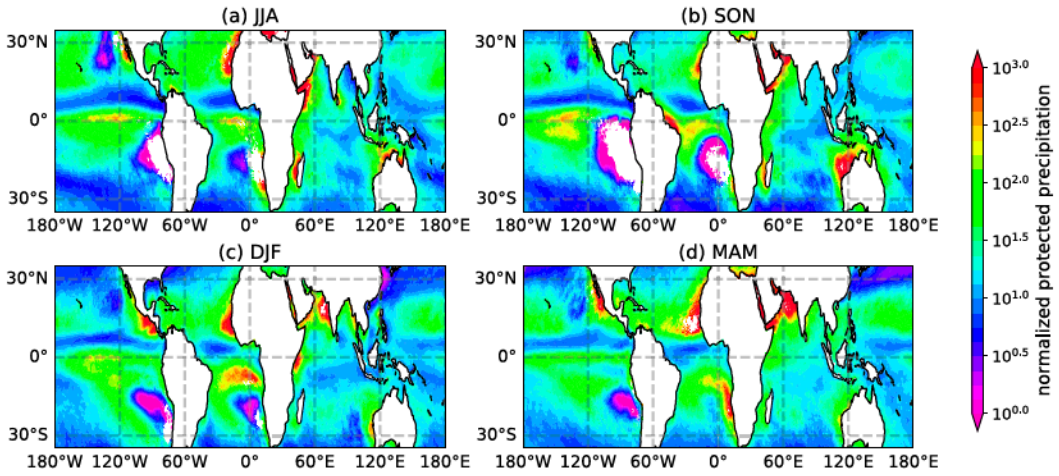

FIG. 4. As in Fig. 3, but for protected precipitation normalized by TRMM 3B42 precipitation. All land regions and ocean regions with mean precipitation less than 10 mm yr^{-1} are masked.

2) *Large protected precipitation and moderate climatological precipitation.* Regions such as the Caribbean, the Gulf of Mexico, the seas of the Maritime Continent, and, to some extent, the northwestern Pacific Ocean all exhibit substantial absolute values of protected precipitation in Fig. 3 (>5 mm h^{-1}). These values exceed the background precipitation by about one order of magnitude (10–30). Such regions are dry air limited, but to a lesser degree than those discussed in the first group.
3) *Large protected protection and large climatological precipitation.* These regions show substantial values in Fig. 3 (>4 mm h^{-1}) but relatively smaller values in Fig. 4, and mostly include the climatologically precipitating oceans: the Indo-Pacific warm pool, and the Atlantic and Pacific ITCZs. These regions are impacted by protection, but the impacts are relatively modest (a factor of ~2–3 in Fig. 4) when compared to the subtropical waters. In such regions, the ambient air is closer to saturation, so convection is relatively less limited by dry air dilution.
4) *Small protected precipitation and small climatological precipitation.* These regions display large values in Fig. 4 (>10^2) but relatively smaller values in Fig. 3. Protecting convection in these regions only yields modest changes in absolute terms (<1 mm h^{-1}), suggesting that they are also influenced by stable temperature profiles. However, even these modest values are sufficient to overwhelm the near-zero background values, suggesting that these locations are severely dry air limited. Examples of such regions are found in the subtropics: on the eastern edge of the subtropical anticyclones and descending zones of the Hadley circulation, poleward of the Pacific and Atlantic ITCZs.

b. Possible drying mechanisms

We briefly discuss a few physical pathways that can suppress free tropospheric and boundary layer humidity in the regions of interest identified above. For warm waters adjoining land regions, one candidate pathway is the advection of dry air from arid land, such as off the West African coast (Zhang and Pennington 2004). Another candidate mechanism is the circulation associated with land–sea thermal contrasts (Yang and Slingo 2001) and coastal orography (Houze 2012) that leads to enhancement of precipitation over coastal land and suppression over neighboring waters (Ogino et al. 2016). For instance, over the shallow seas surrounding the islands of the Maritime Continent, a land–sea circulation is set up by the strong daytime heating of the islands relative to oceans; the subsiding branch of this circulation is known to suppress precipitation over the sea (Neale and Slingo 2003; Mori et al. 2004; Qian 2008). Similar local land–sea dynamics are known to suppress precipitation off the western Mexican coast (Douglas et al. 1993) at the expense of increased precipitation over nearby land. This offshore rainfall signature could be obscured by compensation from strong nocturnal propagation (Mapes et al. 2003; Wu et al. 2009; Li and Carbone 2015) but is clearly strong enough to be seen over many regions. The large values of normalized protected precipitation in such offshore regions suggest that it is the drying that accompanies the subsidence—as opposed to temperature inversions—that limits precipitation.

The proximity of the Caribbean Sea and the Gulf of Mexico to the North American coast suggests potential moisture inhibition due to land–sea dynamics. However, large-scale drying effects from midlatitude and Saharan dry air intrusions (Sun et al. 2008; Dunion 2011), and the southward expansion of the North Atlantic high pressure system (Gamble and Curtis 2008; Martinez et al. 2019) could also be present. Several drying mechanisms can therefore act in combination with the warm surface temperatures (Zavala-Hidalgo et al. 2002; Wang et al. 2006) to produce the disparities between protected and observed precipitation in this region.

Even over the warm oceans, the protected precipitation exceeds observed values by at least a factor of 2, suggesting a role for dry air in shaping the warm ocean precipitation climatology. Plausible sources of drying include dry air intrusions, which are well documented in both regional studies (Numaguti et al. 1995; Mapes and Zuidema 1996; Yoneyama and Parsons 1999; Parsons

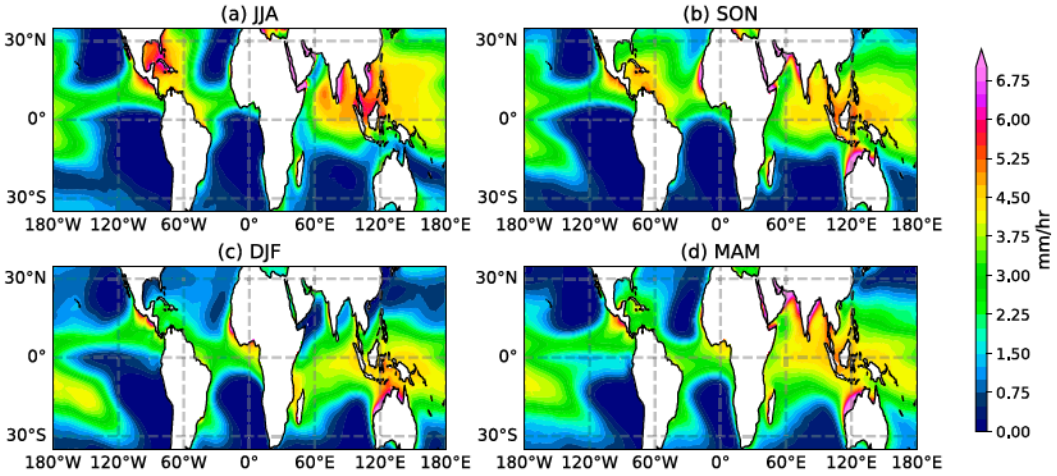

FIG. 5. As in Fig. 3, but for precipitation computed using plume buoyancies protected in the lowest 200 hPa above the surface.

et al. 2000; Yoneyama 2003; Zuidema et al. 2006) and tropics-wide surveys (e.g., Casey et al. 2009). Compared to deep tropical oceans, precipitation is more dry air limited over the subtropical oceans, likely because of subtropical descent zones. For instance, the northwestern Pacific during the boreal summer (Fig. 4a) is moderately dry air limited (normalized protected precipitation ~10) because of the presence of the summertime western Pacific subtropical high (Liu and Wu 2004; Miyasaka and Nakamura 2005). Since the descent strength is weaker under the western and central portions of subtropical highs when compared to the eastern flanks (Rodwell and Hoskins 2001; Liu et al. 2004; Miyasaka and Nakamura 2005), the lower tropospheric temperature structure does not limit the precipitation enhancement under protection (~4.5 mm h^{-1} in Fig. 3).

c. *Relationship to tropical cyclone genesis indices*

The use of undilute buoyancy as an index to diagnose TC genesis can be traced back to Palmén (1948). Other commonly used genesis indices such as the instability index (Gray 1975, 1998; DeMaria et al. 2001) and the potential intensity (Emanuel and Nolan 2004; Camargo et al. 2007b) are implicit measures of protected convection. These indices are used alongside other relevant measures for cyclone genesis such as total cyclonic vorticity and wind shear. A degree of spatial overlap therefore exists between protected precipitation and TC genesis indices. A subset of regions with large protected precipitation and moderate climatological precipitation—the Caribbean Sea, the Gulf of Mexico, and the northwestern Pacific Ocean during the Northern Hemisphere summer—show pronounced signals in both metrics [cf. Fig. 3a with Fig. 1 in Camargo et al. (2007a)]. These connections suggest that combining the protected precipitation metric with a measure of ambient vorticity could possibly create another useful index for TC genesis.

d. *Partial protection*

It is instructive to identify the tropospheric layers in which dilution is most impactful on precipitation—particularly over regions with large protected precipitation. To this end, a partially protected precipitation product is constructed by enforcing protection in only the 200-hPa layer closest to the surface. Figure 5 shows the 200-hPa partially protected precipitation, separated by four seasons. A first-glance analysis is sufficient to infer that the spatial structure in fully protected precipitation (Fig. 3) can be captured with partial protection. In the waters around the Arabian Peninsula during JJA and SON (Figs. 5a,b), protecting only the bottom 200-hPa layer is sufficient to produce precipitation values that largely exceed the background climatology. In JJA and SON, protection in the lowest 200-hPa layer is sufficient to account for over 80% of the fully protected precipitation (not explicitly shown) over the Gulf of Mexico, the Indo-Pacific warm pool, and the Pacific and Atlantic ITCZs. Dilution in a fairly thin lower-tropospheric layer (200 hPa thick) when compared to the full tropospheric depth is therefore sufficient to influence precipitation across the tropics and subtropics. When protection is separately enforced in 100-hPa-thick layers closest to the surface and in the lower free troposphere, the protected precipitation magnitudes in Fig. 3 are not fully recovered (not shown), suggesting that the dry air influence on precipitation spans both these layers.

5. Protected convection in CAM5

a. *Motivations*

We now turn to experiments with CAM5 to investigate if and to what extent the predictions from the empirical analysis in section 4 are borne out in a model with full physics. We proceed with the caveat that some of the results in this section could hinge on the details of parameterized convection in CAM5. We have two primary motivations for the model experiments:

1) The buoyancy relationships from AN18 and S18 imply that regions protected from dry air can generate large precipitation values well in excess of climatology. However, it is a priori unclear to what extent these large precipitation values can be sustained against negative feedbacks. For

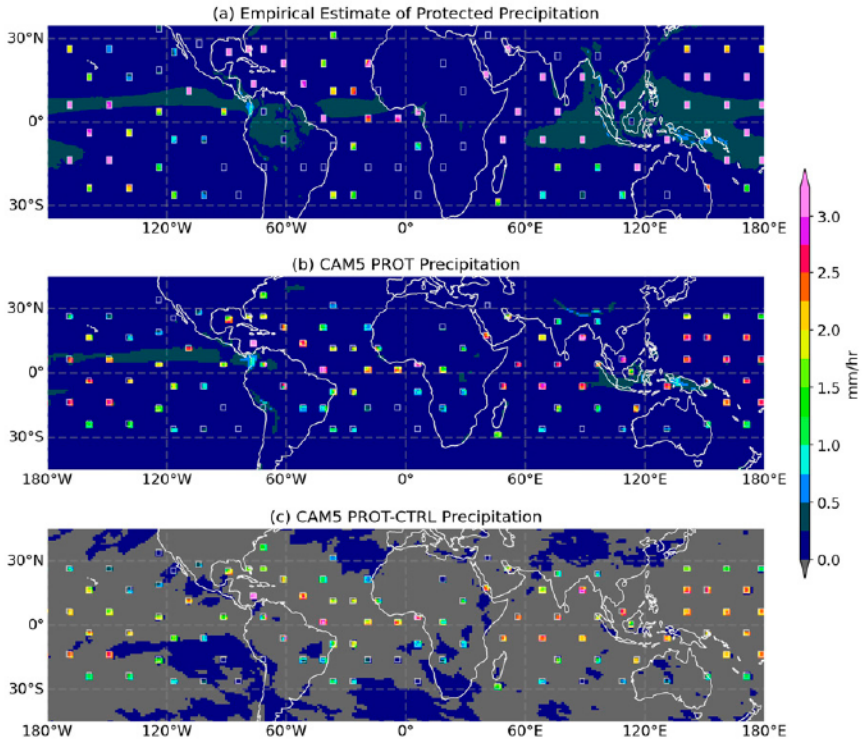

FIG. 6. (a) Protected locations shown in white-edged transparent boxes are arranged in a lattice-like structure. Protected precipitation from Fig. 2a is shown within the protected lattice; mean TRMM 3B42 precipitation is displayed outside the protected pockets. (b) Two-year-averaged precipitation from the CAM5 PROT run with the protected lattice. (c) Difference between (b) and mean precipitation from CTRL for the same period. The gray shading in (c) denotes regions where the mean CTRL precipitation exceeds the mean PROT precipitation. Each pocket contains more than one grid point, so precipitation variations do occur within a single pocket.

instance, in precipitating regions over tropical oceans, the injection of low entropy air into the boundary layer is the leading-order negative feedback on precipitation (Raymond 1995; Emanuel 1995; Adames et al. 2021), which is modeled within the ZM scheme [see Eq. (2) in Zhang and McFarlane 1995]. Other negative feedbacks captured by the model setup include limits imposed by conservation laws on large-scale moisture availability and diabatic heating induced tropospheric warming that reduces CAPE. The use of prescribed SSTs precludes some negative feedbacks such as SST reductions in precipitating regions due to cloud-shading effects. However, for a first check, our model setup is adequate to verify if large precipitation values in protected regions can be sustained over time.

2) An empirical estimate of protected precipitation was not offered over tropical land. This is because factors such as strong surface heating, differences in microphysics (e.g., Matsui et al. 2016; Zipser et al. 2006) and unclear soil moisture feedbacks (e.g., Eltahir 1998; Cook et al. 2006; Hohenegger et al. 2009) are also expected to influence precipitation. The model experiments will be used to examine how protection from dry air influences precipitation over land regions.

b. *Protected precipitation in CAM5*

Protection is directly enforced in the model's convection scheme using the method described in section 2c. Protection is also enforced only within geographically restricted regions termed "protected pockets." Note the difference here from climate model experiments that alter the dilution rates *uniformly* in space (Tokioka et al. 1988; Kim et al. 2011; Hannah and Maloney 2011). Geographically restricting the protection retains the competitive advantage afforded to convection due to spatial variations in dilution rates. While the influence of restricted protection could be examined one pocket at a time, it is efficient both in computation and in presentation to simultaneously examine multiple pockets that are sufficiently separated in space. The pockets used here are ~2° × 2° in size and contain four grid points, each with a nominal resolution ~1° × 1°. These pockets are distributed across the tropics and the subtropics, over both land and ocean regions (denoted by transparent white-edged boxes in Fig. 6a). Initial short experiments with a single protected pocket suggested that this spacing (roughly 1 pocket per 3×10^6 km^2) yields little interference between them. The pockets are also preferentially placed within regions displaying the strongest signal in

protected precipitation from Figs. 2a and 3. Figure 6a shows the precipitation map that we expect a priori from this spatially restricted protection. The precipitation inside protected pockets is the annual mean empirical protected precipitation from Fig. 2a, while the precipitation outside the pockets is the annual mean TRMM 3B42 precipitation. Since predictions for protected precipitation over land were not empirically generated, the precipitation inside the land pockets is the same as the background TRMM 3B42 precipitation.

Figure 6b shows the mean CAM5 precipitation in the standard protected run (PROT) averaged over the first two years. Conforming to our expectation from Fig. 6b, the precipitation is enhanced within the protected lattice—exceeding the CTRL precipitation values by nearly an order of magnitude in many locations. As in the case of empirical protected precipitation, the enhancement is greatest over warm waters. Notably, the pockets over the Red Sea and the Persian Gulf show substantial values of mean protected precipitation ($\sim$2.5 mm h^{-1}), consistent with the empirical results over the same regions. Protection from dilution is less impactful over the strongest subtropical subsidence zones in the east Pacific and Atlantic Oceans, which is also in agreement with the empirical results. The magnitudes of protected precipitation in CAM5 are noticeably weaker than the ERA5 estimates; given the parameterized nature of CAM5 convection, we will not dwell on these quantitative differences.

As anticipated, protection from dilution generates mixed results over land with strong precipitation enhancement over parts of the Amazon, Congo, and the Maritime Continent, and weak to no enhancement in other regions such as Australia, India, and North America. Generally speaking, a protected pocket over land shows a weaker precipitation enhancement than a nearby ocean pocket. Pairs of land–ocean pockets exemplify this dichotomous precipitation response (e.g., Mexico and the Gulf of Mexico, Borneo and the South China Sea, and Congo and the Gulf of Guinea). The difference in mean precipitation between the PROT and CTRL runs are shown in Fig. 6c. The gray shading denotes regions where the CTRL run produced more precipitation than PROT; the shading indicates that regions outside the protected pockets are slightly drier in PROT than in CTRL. The annual mean precipitation values in both the CTRL and PROT runs are the same (3.3 mm day^{-1}), when averaged over the domain displayed in Fig. 6. The primary effect of spatially varying dilution rates is therefore a redistribution of the mean precipitation, where the protected pockets produce substantial rain at the expense of neighboring regions. The reduction over the surrounding region is modest, since wave dynamics spreads the compensating descent over distances on the order of the Rossby deformation radius ($\sim$1000 km), as for any localized heating (Bretherton and Smolarkiewicz 1989). The precipitation within each protected pocket of Fig. 6 is enhanced approximately independently of other pockets. The seasonal variations in protected precipitation noted in Fig. 3 are also approximately reproduced in the PROT run (not shown).

c. *Thermodynamic controls on CAM5 precipitation*

What explains the spatial variation in the intensity of protected precipitation in Fig. 6b, including the land–ocean differences? To further probe this question, we first examine the relationship between precipitation and DCAPE from the ZM scheme. A strong relationship between these two quantities is built into the ZM scheme closure, which dictates that positive DCAPE perturbations on the model grid scale be consumed by subgrid-scale convection (Neale et al. 2008). Note that within protected pockets the closure uses CAPE, which is the protected version of DCAPE. Figure 7a shows the total CAM5 precipitation conditionally averaged by DCAPE (in CTRL) and CAPE (in PROT) only for ocean points within the protected lattice. Figure 7b shows the corresponding figure for land points. The conditional averages are constructed separately for each of the three years (years 1–3) used in the PROT and CTRL runs. A reference pressure depth Δp = 490 hPa is used to scale DCAPE and CAPE such that the units are in meters per second squared (m s^{-2}).

Over the oceans (Fig. 7a) the model precipitation appears to be linearly related to DCAPE (in CTRL) and CAPE (in PROT) over a substantial range. This range extends to much larger values ($\gtrsim$2.5 mm h^{-1}) for PROT than for CTRL precipitation ($\lesssim$1.5 mm h^{-1}). Nonlinearities are introduced at higher CAPE values (>0.2 ms^{-2}) where the PROT precipitation changes sublinearly with CAPE and then flattens. The PROT and CTRL precipitation values lie on the same curve; protection therefore does not greatly impact the CAM5 precipitation relationship to its thermodynamic environment over oceans. Moreover, the precipitation curves in Fig. 7a are fairly invariant from year to year, suggesting a strong constraint from the closure in the ZM scheme. By contrast, the precipitation statistics over the land regions (Fig. 7b) show considerable scatter; the precipitation curves from the PROT run do not coincide with the curves in the CTRL run, and have smaller slopes than the ocean curves in Fig. 7a. Moreover, there is considerable year-to-year variability in the protected precipitation curves. Even though a strong relationship between DCAPE/CAPE and precipitation is built into the ZM scheme, this relationship emerges more robustly over the ocean than over land points. This suggests that factors besides thermodynamic profiles influence precipitation over land in CAM5.

We now check if the knowledge of CAPE (the protected version of DCAPE) alone provides any insight into understanding the spatial variations in Fig. 6b. From the closure in the ZM scheme, we expect some skill to be present in the CAPE values from CTRL in estimating protected precipitation in PROT. To quantify this skill, the precipitation–CAPE relationships (for the PROT run in Figs. 7a,b) from one year are used to predict the protected precipitation for the subsequent year in a cyclic permutation. That is, the protected precipitation curve from year 1 predicts the annual mean precipitation for year 2 using daily-averaged CAPE values from the year 2 CTRL run as inputs. We represent this process by year 1 $\rightarrow$ year 2. Similarly, we also perform year 2 $\rightarrow$ year 3 and year 3 $\rightarrow$ year 1. Figure 7c shows that the precipitation–CAPE estimator over oceans generates reasonable predictions (as measured by the one-to-one line) over most of the oceanic pockets. Considerable scatter exists around the one-to-one line, and the mean precipitation predictor does show a slight tendency to overestimate the protected precipitation magnitudes

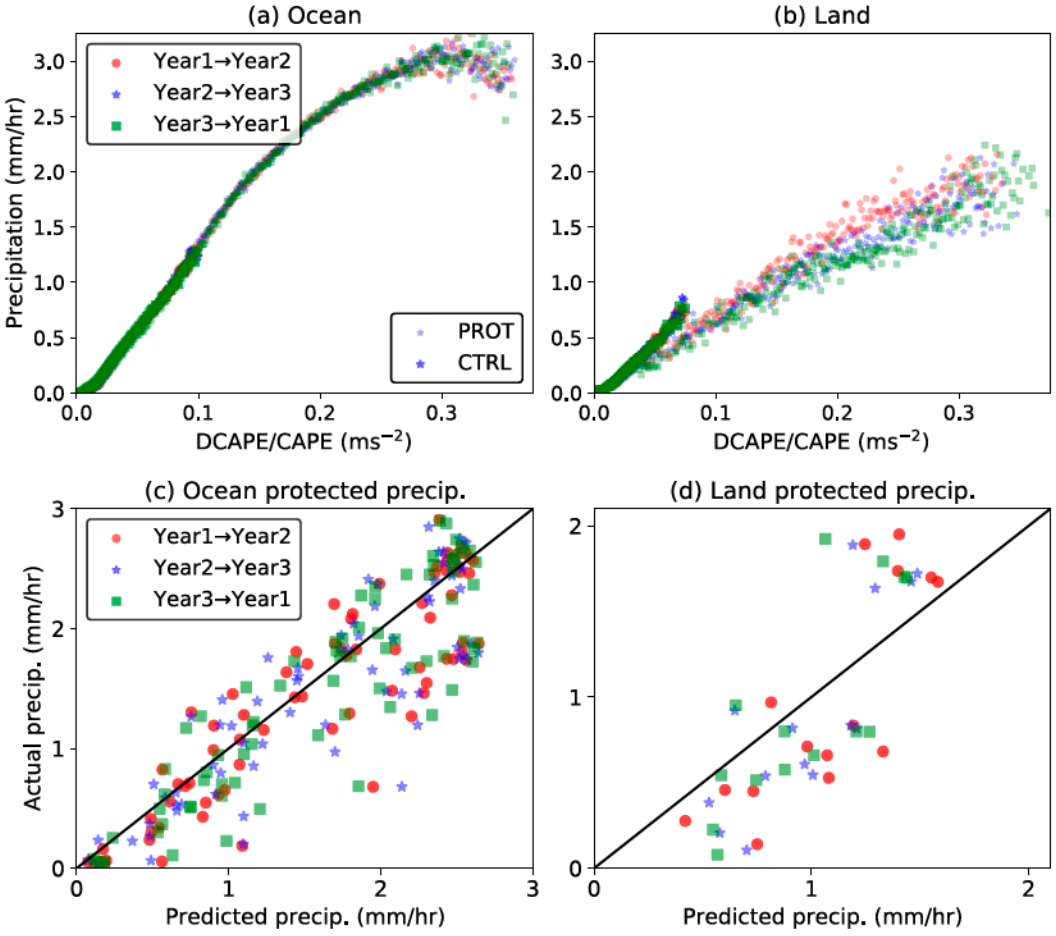

FIG. 7. (a) CAM5 precipitation conditionally averaged by DCAPE (in CTRL) and CAPE (in PROT) for ocean points inside the protected lattice; three separate years for both PROT and CTRL runs are shown. (b) As in (a), but for land points. The scatter between protected precipitation estimated using CTRL and the annual mean protected precipitation from PROT for three different years over the (c) ocean pockets and (d) land pockets. In (c) and (d) Year 1 → Year 2 denotes the precipitation estimated for year 2 using the predictors in year 1 in (a) and (b), respectively, and similarly for Year 2 → Year 3 and Year 3 → Year 1. The one-to-one line is shown in black in both (c) and (d).

over oceans. Over land (Fig. 7d), the precipitation–CAPE predictor can qualitatively capture the protected precipitation, but it overestimates the weak and underestimates the strong protected precipitation values, pointing to an influence from factors besides CAPE. Over both land and ocean, we thus see that the precipitation changes under protection are roughly dictated by the CAPE values, which explains some of the spatial variations—including land–ocean differences—seen in Fig. 6b.

6. Additional CAM5 experiments

a. *Uniform microphysics and weaker protection*

The PROT run provides an affirmative answer—within the scope of parameterized convection—to our queries as to (i) whether precipitation is indeed stronger under protection, and (ii) if it can be sustained over time against local negative feedbacks. In this section, two additional tests are used to probe these results. The first test uses the C0EXP run with identical precipitation efficiency values over land and ocean. Figure 6b shows that protected precipitation over land is generally weaker than over oceans, which is only partly explained by smaller CAPE values over land (Fig. 7). The C0EXP run is used to ask whether differences in the treatment of microphysics over land within the ZM scheme can also account for the weaker values of land protected precipitation. The second test uses the ENTOFF run to check if enforcing weaker protection than in PROT, with stronger local negative feedbacks on the boundary layer due to re-evaporation, and updraft and downdraft dilution negates the effects of protection. As seen from Fig. 8, in both cases the differences from PROT run are of degree and not of kind. In Fig. 8a, using the same precipitation efficiency only minimally alters the character of protected precipitation over land. A few pockets such as the ones over the Congo and Borneo display an

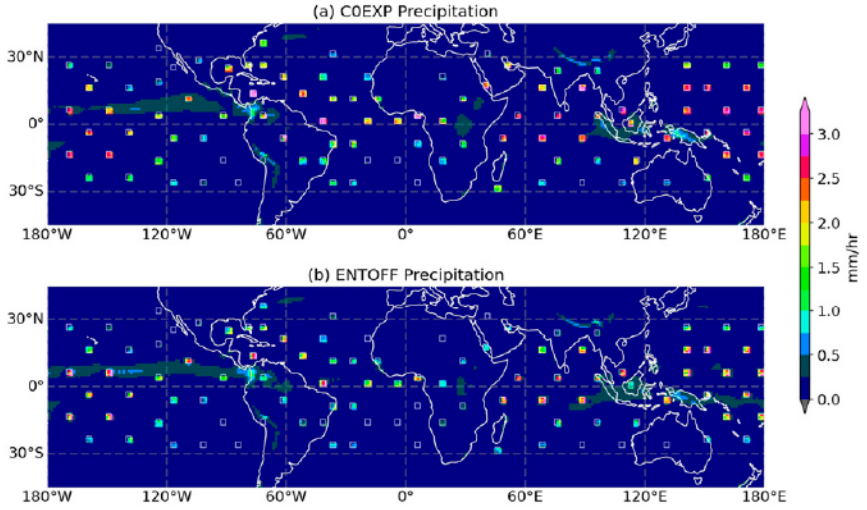

FIG. 8. As in Fig. 6b, but for the (a) C0EXP and (b) ENTOFF runs.

enhancement in precipitation (not explicitly shown) when compared to Fig. 6b, but the general lack of enhancement over other protected land pockets remains. This suggests that differing treatments of microphysics in the ZM scheme are one among several factors—besides CAPE—that are responsible for land–ocean differences in protected precipitation. In Fig. 8b, enforcing protection by only switching off entrainment in the closure slightly reduces the magnitude of protected precipitation, but this reduction still pales in comparison to the enhancement over background values. Even over the marine desert environments of the Red Sea and the Persian Gulf, the competitive advantage offered by the protection in the closure is sufficient to overcome increased negative feedbacks on the boundary layer, and enhance the magnitudes of protected precipitation relative to background values.

b. *Protected precipitation in a warmer climate*

The results from CAM5 demonstrate that protecting regions from unsaturated ambient air can produce large precipitation amounts. This observation raises the prospect that protected pockets could serve as prototypes for the study of extreme precipitation. This possibility is supported by scaling theories for precipitation extremes, where the physical picture is one of undilute plumes rising through saturated atmospheres (O'Gorman and Schneider 2009; Muller et al. 2011; Loriaux et al. 2013). The pockets could also mimic the protection available within the inner core of TCs (Braun et al. 2012; Kimball 2006; Fritz and Wang 2013). To illustrate some of the behavior that could be investigated under this interpretation, we examine the changes to protected precipitation under a uniform 2-K SST warming. A robust prediction under global warming is the increase in extreme precipitation in general (Pall et al. 2007; Kharin et al. 2013; Pendergrass and Hartmann 2014; O'Gorman 2015), and precipitation from TCs in particular (Knutson et al. 2010; Wang et al. 2014; Knutson et al. 2020). If protected pockets are useful prototypes for the study of extreme precipitation, then the a priori expectation is that protected precipitation amounts will increase under warming.

Figure 9a shows the difference between the precipitation changes in the CLIM2K PROT and CLIM PROT runs relative to their corresponding CTRL runs. This double difference accounts for changes in CTRL runs under warming, and emphasizes the changes to the protected regions. It is quite clear

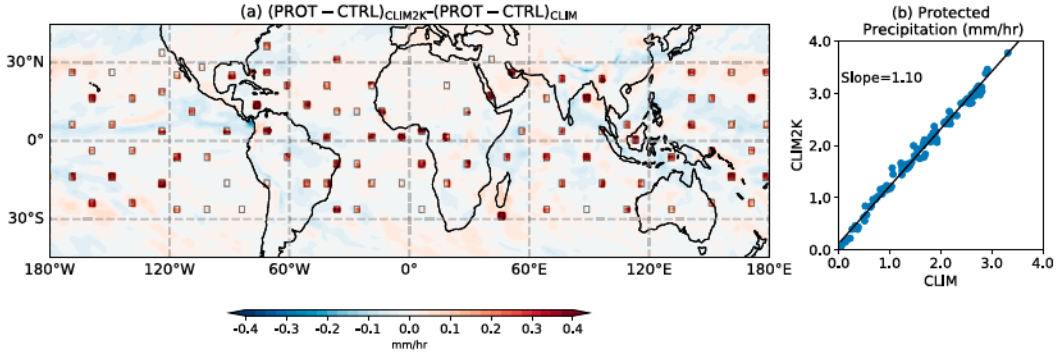

FIG. 9. (a) The difference between precipitation changes under protection relative to control in the CLIM2K and CLIM runs. (b) Scatterplot between protected precipitation in the CLIM and CLIM2K runs.

that the protected precipitation increases under warming, with the largest absolute differences occurring over the most intensely precipitating pockets. Figure 9b shows the precipitation within protected pockets in the CLIM2K run regressed against the corresponding values in the CLIM run. The intensification of the protected precipitation under warming is nearly uniform at an average rate of ~5% K^{-1}, as inferred from the regression slope. The rate of change in protected precipitation is slightly less than the Clausius–Clapeyron scaling rate (7% K^{-1}); this departure possibly arising from saturation specific humidity profile changes along a moist adiabat (O'Gorman and Schneider 2009). The general behavior of protected precipitation under warming supports the possibility that in certain situations, protected pockets can isolate the physics of extreme precipitation. A useful future step would be to check if protected pockets behave similarly under warming in models that resolve convection.

7. Summary and discussion

a. Summary

We infer the influence of dry air on tropical precipitation by first estimating the protected precipitation that would arise in the absence of dilution, and then comparing these values to the observed precipitation. To produce the protected precipitation estimates, we leverage the empirical precipitation–buoyancy relationship alongside buoyancies from an entraining plume model that entrains saturated environmental air. The protected precipitation field normalized by the observed precipitation is used to highlight regions where precipitation is greatly limited by the presence of dry air. Equatorward of 35° latitude, the most dry air limited regions are subtropical warm waters adjoining land. The waters surrounding the Arabian Peninsula are severely dry air limited but also display conspicuously large values of protected precipitation. Regions including the Gulf of Mexico, the Caribbean Sea, the Maritime Continent, and the northwestern Pacific Ocean all display substantial values of protected precipitation, but are more moderately dry air limited. The ocean regions of the deep tropics are among the least dry air limited owing to small ambient subsaturation values; even in these regions protecting convection yields precipitation values that are at least twice as large as observed. Protecting regions on the eastern edge of subtropical highs only yields minimal increases in precipitation values, pointing to additional limiting influences from capping inversions. Much of the dry air influence on precipitation is ascribed to dilution in a 200-hPa-thick layer overlying the surface.

Experiments with CAM5 are used to illustrate the effects of directly shielding parameterized convection from dilution in small regions of the model grid. The model shows a strong enhancement of precipitation within these protected pockets, and a slight precipitation decrease everywhere outside. Ocean points in the model show greater increases in protected precipitation, when compared to the land points at similar latitudes. Under a uniform SST warming, the protected precipitation values in CAM5 intensify, much like the projected increases for precipitation extremes.

b. Meteorological protection

Given the considerable precipitation enhancement that arises from artificial protection, it is worth detailing some meteorological situations that enforce natural protection—and their consequences. For instance, closely spaced convective elements mutually shield themselves from dilution (Feng et al. 2015; Moser and Lasher-Trapp 2018), with the consequence that large organized convective systems are more likely to survive in a drier environment than scattered convection (Mapes et al. 2017). Small-scale vortical hot towers (Montgomery et al. 2006) are thought to possess intense cyclonic vorticity that makes them more resistant to lateral entrainment, with tropical cyclogenesis a possible consequence. In fully developed cyclones, the inertial stability of the cyclonic circulation can also shield a moist envelope in the inner core from dilution (Braun et al. 2012), enhancing the longevity of such systems. In the subtropics, partial protection from dilution can take the form of lower tropospheric moisture influx from the tropics (McGuirk et al. 1988; Zhu and Newell 1998; Guan and Waliser 2015). In regions that are greatly dry air limited, such moisture injections can produce extreme precipitation events (de Vries et al. 2013, 2018). It could be useful to estimate the degree of protection present in each of these examples, using the normalized protected precipitation metric. Quantifying this degree of protection in weather systems could aid forecasts by predicting precipitation amounts using only temperature information. Similarities in the physical picture and behavior under warming point to the potential utility of protected-pocket experiments to study precipitation extremes resulting from convection in a saturated environment. Such an approach could help us better understand the physics underlying regional patterns of precipitation extremes (Fischer et al. 2013; Pfahl et al. 2017).

c. Land–ocean differences in protected convection

Protecting convection over CAM5 land generally results in weaker precipitation when compared to the nearest ocean pocket. In relation to naturally protected convection, the decay of landfalling tropical cyclones (Tuleya and Kurihara 1978; Tuleya 1994) exemplifies this land–ocean contrast. Protecting convection over CAM5 land regions also generates a less predictable precipitation response, pointing to a weakened link between CAPE and protected precipitation on daily time scales. For a given free tropospheric temperature, the undilute buoyancy is strongly determined by the boundary layer moist enthalpy, which is in turn tied to the surface energy budget. This budget differs substantially between land and ocean (Sutton et al. 2007; Andrews et al. 2009), particularly on the diurnal time scale (Betts and Jakob 2002), and is therefore comparable to the fast time scales of convection. The variability in the surface properties tends to make land convection more complex in terms of whether it is "surface limited" versus dry air limited.

Finally, we emphasize that our experiments with parameterized convection constitute a preliminary examination of how protection affects precipitation. More realistic tests to isolate the effects of protection in cloud-resolving modeling

and large-eddy simulations are worthy targets for future efforts.

Acknowledgments. The authors were supported by National Science Foundation Grant AGS-1936810. We thank S. Sahany for discussions on unpublished experiments with localized reductions of entrainment. Comments from Christian Jakob and two anonymous reviewers helped improve an early version of this paper. The modified Zhang–McFarlane scheme codes that enforce protection in CAM5 can be accessed at https://github.com/ahmedfiaz/Protected_convection_ZM.

REFERENCES

Adames, Á. F., S. W. Powell, F. Ahmed, V. C. Mayta, and J. D. Neelin, 2021: Tropical precipitation evolution in a buoyancy-budget framework. *J. Atmos. Sci.*, **78**, 509–528, https://doi.org/10.1175/JAS-D-20-0074.1.

Ahmed, F., and C. Schumacher, 2015: Convective and stratiform components of the precipitation–moisture relationship. *Geophys. Res. Lett.*, **42**, 10 453–10 462, https://doi.org/10.1002/2015GL066957.

——, and ——, 2017: Geographical differences in the tropical precipitation–moisture relationship and rain intensity onset. *Geophys. Res. Lett.*, **44**, 1114–1122, https://doi.org/10.1002/2016GL071980.

——, and J. D. Neelin, 2018: Reverse engineering the tropical precipitation–buoyancy relationship. *J. Atmos. Sci.*, **75**, 1587–1608, https://doi.org/10.1175/JAS-D-17-0333.1.

——, Á. F. Adames, and J. D. Neelin, 2020: Deep convective adjustment of temperature and moisture. *J. Atmos. Sci.*, **77**, 2163–2186, https://doi.org/10.1175/JAS-D-19-0227.1.

Almazroui, M., 2011: Calibration of TRMM rainfall climatology over Saudi Arabia during 1998–2009. *Atmos. Res.*, **99**, 400–414, https://doi.org/10.1016/j.atmosres.2010.11.006.

——, M. Nazrul Islam, H. Athar, P. D. Jones, and M. A. Rahman, 2012: Recent climate change in the Arabian Peninsula: Annual rainfall and temperature analysis of Saudi Arabia for 1978–2009. *Int. J. Climatol.*, **32**, 953–966, https://doi.org/10.1002/joc.3446.

Andrews, T., P. M. Forster, and J. M. Gregory, 2009: A surface energy perspective on climate change. *J. Climate*, **22**, 2557–2570, https://doi.org/10.1175/2008JCLI2759.1.

Austin, J. M., 1948: A note on cumulus growth in a nonsaturated environment. *J. Meteor.*, **5**, 103–107, https://doi.org/10.1175/1520-0469(1948)005<0103:ANOCGI>2.0.CO;2.

Becker, T., C. S. Bretherton, C. Hohenegger, and B. Stevens, 2018: Estimating bulk entrainment with unaggregated and aggregated convection. *Geophys. Res. Lett.*, **45**, 455–462, https://doi.org/10.1002/2017GL076640.

Bergemann, M., and C. Jakob, 2016: How important is tropospheric humidity for coastal rainfall in the tropics? *Geophys. Res. Lett.*, **43**, 5860–5868, https://doi.org/10.1002/2016GL069255.

Betts, A. K., 1975: Parametric interpretation of trade-wind cumulus budget studies. *J. Atmos. Sci.*, **32**, 1934–1945, https://doi.org/10.1175/1520-0469(1975)032<1934:PIOTWC>2.0.CO;2.

——, and C. Jakob, 2002: Evaluation of the diurnal cycle of precipitation, surface thermodynamics, and surface fluxes in the ECMWF model using LBA data. *J. Geophys. Res.*, **107**, 8045, https://doi.org/10.1029/2001JD000427.

Bluestein, H. B., E. W. McCaul, G. P. Byrd, and G. R. Woodall, 1988: Mobile sounding observations of a tornadic storm near the dryline: The Canadian, Texas storm of 7 May 1986. *Mon. Wea. Rev.*, **116**, 1790–1804, https://doi.org/10.1175/1520-0493(1988)116<1790:MSOOAT>2.0.CO;2.

Braun, S. A., J. A. Sippel, and D. S. Nolan, 2012: The impact of dry midlevel air on hurricane intensity in idealized simulations with no mean flow. *J. Atmos. Sci.*, **69**, 236–257, https://doi.org/10.1175/JAS-D-10-05007.1.

Bretherton, C. S., and P. K. Smolarkiewicz, 1989: Gravity waves, compensating subsidence and detrainment around cumulus clouds. *J. Atmos. Sci.*, **46**, 740–759, https://doi.org/10.1175/1520-0469(1989)046<0740:GWCSAD>2.0.CO;2.

——, M. E. Peters, and L. E. Back, 2004: Relationships between water vapor path and precipitation over the tropical oceans. *J. Climate*, **17**, 1517–1528, https://doi.org/10.1175/1520-0442(2004)017<1517:RBWVPA>2.0.CO;2.

Brown, R. G., and C. Zhang, 1997: Variability of midtropospheric moisture and its effect on cloud-top height distribution during TOGA COARE. *J. Atmos. Sci.*, **54**, 2760–2774, https://doi.org/10.1175/1520-0469(1997)054<2760:VOMMAI>2.0.CO;2.

Bryan, G. H., J. C. Wyngaard, and J. M. Fritsch, 2003: Resolution requirements for the simulation of deep moist convection. *Mon. Wea. Rev.*, **131**, 2394–2416, https://doi.org/10.1175/1520-0493(2003)131<2394:RRFTSO>2.0.CO;2.

Camargo, S. J., K. A. Emanuel, and A. H. Sobel, 2007a: Use of a genesis potential index to diagnose ENSO effects on tropical cyclone genesis. *J. Climate*, **20**, 4819–4834, https://doi.org/10.1175/JCLI4282.1.

——, A. W. Robertson, S. J. Gaffney, P. Smyth, and M. Ghil, 2007b: Cluster analysis of typhoon tracks. Part II: Large-scale circulation and ENSO. *J. Climate*, **20**, 3654–3676, https://doi.org/10.1175/JCLI4203.1.

Casey, S. P., A. E. Dessler, and C. Schumacher, 2009: Five-year climatology of midtroposphere dry air layers in warm tropical ocean regions as viewed by AIRS/Aqua. *J. Appl. Meteor. Climatol.*, **48**, 1831–1842, https://doi.org/10.1175/2009JAMC2099.1.

Cess, R. D., and Coauthors, 1990: Intercomparison and interpretation of climate feedback processes in 19 atmospheric general circulation models. *J. Geophys. Res.*, **95**, 16 601–16 615, https://doi.org/10.1029/JD095iD10p16601.

——, and Coauthors, 1996: Cloud feedback in atmospheric general circulation models: An update. *J. Geophys. Res.*, **101**, 12 791–12 794, https://doi.org/10.1029/96JD00822.

Chaidez, V., D. Dreano, S. Agusti, C. M. Duarte, and I. Hoteit, 2017: Decadal trends in Red Sea maximum surface temperature. *Sci. Rep.*, **7**, 8144, https://doi.org/10.1038/s41598-017-08146-z.

Cook, B. I., G. B. Bonan, and S. Levis, 2006: Soil moisture feedbacks to precipitation in southern Africa. *J. Climate*, **19**, 4198–4206, https://doi.org/10.1175/JCLI3856.1.

Davies, L., C. Jakob, P. May, V. Kumar, and S. Xie, 2013: Relationships between the large-scale atmosphere and the small-scale convective state for Darwin, Australia. *J. Geophys. Res. Atmos.*, **118**, 11 534–11 545, https://doi.org/10.1002/jgrd.50645.

Davies-Jones, R. P., 1974: Discussion of measurements inside high-speed thunderstorm updrafts. *J. Appl. Meteor.*, **13**, 710–717, https://doi.org/10.1175/1520-0450(1974)013<0710:DOMIHS>2.0.CO;2.

Dawe, J. T., and P. H. Austin, 2011: The influence of the cloud shell on tracer budget measurements of LES cloud entrainment. *J. Atmos. Sci.*, **68**, 2909–2920, https://doi.org/10.1175/2011JAS3658.1.

DeMaria, M., J. A. Knaff, and B. H. Connell, 2001: A tropical cyclone genesis parameter for the tropical Atlantic. *Wea. Forecasting*, **16**, 219–233, https://doi.org/10.1175/1520-0434(2001)016<0219:ATCGPF>2.0.CO;2.

de Vries, A. J., E. Tyrlis, D. Edry, S. O. Krichak, B. Steil, and J. Lelieveld, 2013: Extreme precipitation events in the Middle East: Dynamics of the active Red Sea trough. *J. Geophys. Res. Atmos.*, **118**, 7087–7108, https://doi.org/10.1002/jgrd.50569.

——, H. G. Ouwersloot, S. B. Feldstein, M. Riemer, A. M. El Kenawy, M. F. McCabe, and J. Lelieveld, 2018: Identification of tropical–extratropical interactions and extreme precipitation events in the Middle East based on potential vorticity and moisture transport. *J. Geophys. Res. Atmos.*, **123**, 861–881, https://doi.org/10.1002/2017JD027587.

Douglas, M. W., R. A. Maddox, K. Howard, and S. Reyes, 1993: The Mexican monsoon. *J. Climate*, **6**, 1665–1677, https://doi.org/10.1175/1520-0442(1993)006<1665:TMM>2.0.CO;2.

Dunion, J. P., 2011: Rewriting the climatology of the tropical North Atlantic and Caribbean Sea atmosphere. *J. Climate*, **24**, 893–908, https://doi.org/10.1175/2010JCLI3496.1.

Dunkerton, T. J., M. Montgomery, and Z. Wang, 2009: Tropical cyclogenesis in a tropical wave critical layer: Easterly waves. *Atmos. Chem. Phys.*, **9**, 5587–5646, https://doi.org/10.5194/ACP-9-5587-2009.

Eltahir, E. A., 1998: A soil moisture–rainfall feedback mechanism: 1. Theory and observations. *Water Resour. Res.*, **34**, 765–776, https://doi.org/10.1029/97WR03499.

Emanuel, K. A., 1994: *Atmospheric Convection*. Oxford University, 590 pp.

——, 1995: The behavior of a simple hurricane model using a convective scheme based on subcloud-layer entropy equilibrium. *J. Atmos. Sci.*, **52**, 3960–3968, https://doi.org/10.1175/1520-0469(1995)052<3960:TBOASH>2.0.CO;2.

——, 2019: Inferences from simple models of slow, convectively coupled processes. *J. Atmos. Sci.*, **76**, 195–208, https://doi.org/10.1175/JAS-D-18-0090.1.

——, and D. S. Nolan, 2004: Tropical cyclone activity and the global climate system. *26th Conf. on Hurricanes and Tropical Meteorology*, Miami, FL, Amer. Meteor. Soc., 240–241.

Feng, Z., S. Hagos, A. K. Rowe, C. D. Burleyson, M. N. Martini, and S. P. de Szoeke, 2015: Mechanisms of convective cloud organization by cold pools over tropical warm ocean during the AMIE/DYNAMO field campaign. *J. Adv. Model. Earth Syst.*, **7**, 357–381, https://doi.org/10.1002/2014MS000384.

Ferrier, B. S., and R. A. Houze, 1989: One-dimensional time-dependent modeling of gate cumulonimbus convection. *J. Atmos. Sci.*, **46**, 330–352, https://doi.org/10.1175/1520-0469(1989)046<0330:ODTDMO>2.0.CO;2.

Fierro, A. O., J. Simpson, M. A. LeMone, J. M. Straka, and B. F. Smull, 2009: On how hot towers fuel the Hadley cell: An observational and modeling study of line-organized convection in the equatorial trough from TOGA COARE. *J. Atmos. Sci.*, **66**, 2730–2746, https://doi.org/10.1175/2009JAS3017.1.

Fischer, E. M., U. Beyerle, and R. Knutti, 2013: Robust spatially aggregated projections of climate extremes. *Nat. Climate Change*, **3**, 1033–1038, https://doi.org/10.1038/nclimate2051.

Fritz, C., and Z. Wang, 2013: A numerical study of the impacts of dry air on tropical cyclone formation: A development case and a nondevelopment case. *J. Atmos. Sci.*, **70**, 91–111, https://doi.org/10.1175/JAS-D-12-018.1.

Gamble, D. W., and S. Curtis, 2008: Caribbean precipitation: Review, model and prospect. *Prog. Phys. Geogr.*, **32**, 265–276, https://doi.org/10.1177/0309133308096027.

Gray, W. M., 1975: Tropical cyclone genesis. Dept. of Atmos. Sci. Paper 234, Colorado State University, 121 pp., https://mountainscholar.org/bitstream/handle/10217/247/0234_Bluebook.pdf;sequence=1.

——, 1998: The formation of tropical cyclones. *Meteor. Atmos. Phys.*, **67**, 37–69, https://doi.org/10.1007/BF01277501.

Guan, B., and D. E. Waliser, 2015: Detection of atmospheric rivers: Evaluation and application of an algorithm for global studies. *J. Geophys. Res. Atmos.*, **120**, 12 514–12 535, https://doi.org/10.1002/2015JD024257.

Hannah, W. M., 2017: Entrainment versus dilution in tropical deep convection. *J. Atmos. Sci.*, **74**, 3725–3747, https://doi.org/10.1175/JAS-D-16-0169.1.

——, and E. D. Maloney, 2011: The role of moisture–convection feedbacks in simulating the Madden–Julian oscillation. *J. Climate*, **24**, 2754–2770, https://doi.org/10.1175/2011JCLI3803.1.

Hersbach, H., and Coauthors, 2020: The ERA5 global reanalysis. *Quart. J. Roy. Meteor. Soc.*, **146**, 1999–2049, https://doi.org/10.1002/qj.3803.

Hohenegger, C., P. Brockhaus, C. S. Bretherton, and C. Schär, 2009: The soil moisture–precipitation feedback in simulations with explicit and parameterized convection. *J. Climate*, **22**, 5003–5020, https://doi.org/10.1175/2009JCLI2604.1.

Holloway, C. E., and J. D. Neelin, 2009: Moisture vertical structure, column water vapor, and tropical deep convection. *J. Atmos. Sci.*, **66**, 1665–1683, https://doi.org/10.1175/2008JAS2806.1.

Houghton, H. G., and H. E. Cramer, 1951: A theory of entrainment in convective currents. *J. Meteor.*, **8**, 95–102, https://doi.org/10.1175/1520-0469(1951)008<0095:ATOEIC>2.0.CO;2.

Houze, R. A., 2012: Orographic effects on precipitating clouds. *Rev. Geophys.*, **50**, RG1001, https://doi.org/10.1029/2011RG000365.

Huffman, G. J., and Coauthors, 2007: The TRMM Multisatellite Precipitation Analysis (TMPA): Quasi-global, multiyear, combined-sensor precipitation estimates at fine scales. *J. Hydrometeor.*, **8**, 38–55, https://doi.org/10.1175/JHM560.1.

Jakob, C., and A. P. Siebesma, 2003: A new subcloud model for mass-flux convection schemes: Influence on triggering, updraft properties, and model climate. *Mon. Wea. Rev.*, **131**, 2765–2778, https://doi.org/10.1175/1520-0493(2003)131<2765:ANSMFM>2.0.CO;2.

Jensen, M. P., and A. D. Del Genio, 2006: Factors limiting convective cloud-top height at the ARM Nauru Island climate research facility. *J. Climate*, **19**, 2105–2117, https://doi.org/10.1175/JCLI3722.1.

Kharin, V. V., F. Zwiers, X. Zhang, and M. Wehner, 2013: Changes in temperature and precipitation extremes in the CMIP5 ensemble. *Climatic Change*, **119**, 345–357, https://doi.org/10.1007/s10584-013-0705-8.

Kim, D., A. H. Sobel, E. D. Maloney, D. M. W. Frierson, and I.-S. Kang, 2011: A systematic relationship between intraseasonal variability and mean state bias in AGCM simulations. *J. Climate*, **24**, 5506–5520, https://doi.org/10.1175/2011JCLI4177.1.

Kimball, S. K., 2006: A modeling study of hurricane landfall in a dry environment. *Mon. Wea. Rev.*, **134**, 1901–1918, https://doi.org/10.1175/MWR3155.1.

Kingsmill, D. E., and R. A. Houze, 1999: Thermodynamic characteristics of air flowing into and out of precipitating convection over the west Pacific warm pool. *Quart. J. Roy. Meteor. Soc.*, **125**, 1209–1229, https://doi.org/10.1002/qj.1999.49712555606.

Knutson, T. R., and Coauthors, 2010: Tropical cyclones and climate change. *Nat. Geosci.*, **3**, 157–163, https://doi.org/10.1038/ngeo779.

——, and Coauthors, 2020: Tropical cyclones and climate change assessment: Part II: Projected response to anthropogenic warming. *Bull. Amer. Meteor. Soc.*, **101**, E303–E322, https://doi.org/10.1175/BAMS-D-18-0194.1.

Kumar, V. V., C. Jakob, A. Protat, C. R. Williams, and P. T. May, 2015: Mass-flux characteristics of tropical cumulus clouds from wind profiler observations at Darwin, Australia. *J. Atmos. Sci.*, **72**, 1837–1855, https://doi.org/10.1175/JAS-D-14-0259.1.

Kuo, Y.-H., K. A. Schiro, and J. D. Neelin, 2018: Convective transition statistics over tropical oceans for climate model diagnostics: Observational baseline. *J. Atmos. Sci.*, **75**, 1553–1570, https://doi.org/10.1175/JAS-D-17-0287.1.

Li, Y., and R. E. Carbone, 2015: Offshore propagation of coastal precipitation. *J. Atmos. Sci.*, **72**, 4553–4568, https://doi.org/10.1175/JAS-D-15-0104.1.

Liu, Y., and G. Wu, 2004: Progress in the study on the formation of the summertime subtropical anticyclone. *Adv. Atmos. Sci.*, **21**, 322–342, https://doi.org/10.1007/BF02915562.

——, ——, and R. Ren, 2004: Relationship between the subtropical anticyclone and diabatic heating. *J. Climate*, **17**, 682–698, https://doi.org/10.1175/1520-0442(2004)017<0682:RBTSAA>2.0.CO;2.

Loriaux, J. M., G. Lenderink, S. R. De Roode, and A. P. Siebesma, 2013: Understanding convective extreme precipitation scaling using observations and an entraining plume model. *J. Atmos. Sci.*, **70**, 3641–3655, https://doi.org/10.1175/JAS-D-12-0317.1.

Louf, V., C. Jakob, A. Protat, M. Bergemann, and S. Narsey, 2019: The relationship of cloud number and size with their large-scale environment in deep tropical convection. *Geophys. Res. Lett.*, **46**, 9203–9212, https://doi.org/10.1029/2019GL083964.

Mapes, B. E., and P. Zuidema, 1996: Radiative-dynamical consequences of dry tongues in the tropical troposphere. *J. Atmos. Sci.*, **53**, 620–638, https://doi.org/10.1175/1520-0469(1996)053<0620:RDCODT>2.0.CO;2.

——, T. T. Warner, and M. Xu, 2003: Diurnal patterns of rainfall in northwestern South America. Part III: Diurnal gravity waves and nocturnal convection offshore. *Mon. Wea. Rev.*, **131**, 830–844, https://doi.org/10.1175/1520-0493(2003)131<0830:DPORIN>2.0.CO;2.

——, A. S. Chandra, Z. Kuang, and P. Zuidema, 2017: Importance profiles for water vapor. *Shallow Clouds, Water Vapor, Circulation, and Climate Sensitivity*, Springer, 183–197.

Martinez, C., L. Goddard, Y. Kushnir, and M. Ting, 2019: Seasonal climatology and dynamical mechanisms of rainfall in the Caribbean. *Climate Dyn.*, **53**, 825–846, https://doi.org/10.1007/s00382-019-04616-4.

Matsui, T., J.-D. Chern, W.-K. Tao, S. Lang, M. Satoh, T. Hashino, and T. Kubota, 2016: On the land–ocean contrast of tropical convection and microphysics statistics derived from TRMM satellite signals and global storm-resolving models. *J. Hydrometeor.*, **17**, 1425–1445, https://doi.org/10.1175/JHM-D-15-0111.1.

McGuirk, J. P., A. H. Thompson, and J. R. Schaefer, 1988: An eastern Pacific tropical plume. *Mon. Wea. Rev.*, **116**, 2505–2521, https://doi.org/10.1175/1520-0493(1988)116<2505:AEPTP>2.0.CO;2.

Mechem, D. B., R. A. Houze Jr., and S. S. Chen, 2002: Layer inflow into precipitating convection over the western tropical Pacific. *Quart. J. Roy. Meteor. Soc.*, **128**, 1997–2030, https://doi.org/10.1256/003590002320603502.

Miyasaka, T., and H. Nakamura, 2005: Structure and formation mechanisms of the Northern Hemisphere summertime subtropical highs. *J. Climate*, **18**, 5046–5065, https://doi.org/10.1175/JCLI3599.1.

Molinari, J., D. M. Romps, D. Vollaro, and L. Nguyen, 2012: CAPE in tropical cyclones. *J. Atmos. Sci.*, **69**, 2452–2463, https://doi.org/10.1175/JAS-D-11-0254.1.

Montgomery, M. T., M. E. Nicholls, T. A. Cram, and A. B. Saunders, 2006: A vortical hot tower route to tropical cyclogenesis. *J. Atmos. Sci.*, **63**, 355–386, https://doi.org/10.1175/JAS3604.1.

——, L. Lussier III, R. Moore, and Z. Wang, 2010: The genesis of Typhoon Nuri as observed during the Tropical Cyclone Structure 2008 (TCS-08) field experiment–Part 1: The role of the easterly wave critical layer. *Atmos. Chem. Phys.*, **10**, 9879–9900, https://doi.org/10.5194/acp-10-9879-2010.

Mori, S., and Coauthors, 2004: Diurnal land–sea rainfall peak migration over Sumatera Island, Indonesian Maritime Continent, observed by TRMM satellite and intensive rawinsonde soundings. *Mon. Wea. Rev.*, **132**, 2021–2039, https://doi.org/10.1175/1520-0493(2004)132<2021:DLRPMO>2.0.CO;2.

Morrison, H., J. M. Peters, A. C. Varble, W. M. Hannah, and S. E. Giangrande, 2020: Thermal chains and entrainment in cumulus updrafts. Part I: Theoretical description. *J. Atmos. Sci.*, **77**, 3637–3660, https://doi.org/10.1175/JAS-D-19-0243.1.

Moser, D. H., and S. Lasher-Trapp, 2018: Cloud-spacing effects upon entrainment and rainfall along a convective line. *J. Appl. Meteor. Climatol.*, **57**, 1865–1882, https://doi.org/10.1175/JAMC-D-17-0363.1.

Muller, C. J., P. A. O'Gorman, and L. E. Back, 2011: Intensification of precipitation extremes with warming in a cloud-resolving model. *J. Climate*, **24**, 2784–2800, https://doi.org/10.1175/2011JCLI3876.1.

Neale, R. B., and J. Slingo, 2003: The Maritime Continent and its role in the global climate: A GCM study. *J. Climate*, **16**, 834–848, https://doi.org/10.1175/1520-0442(2003)016<0834:TMCAIR>2.0.CO;2.

——, J. H. Richter, and M. Jochum, 2008: The impact of convection on ENSO: From a delayed oscillator to a series of events. *J. Climate*, **21**, 5904–5924, https://doi.org/10.1175/2008JCLI2244.1.

——, and Coauthors, 2012: Description of the NCAR Community Atmosphere Model (CAM 5.0). NCAR Tech. Note NCAR/TN-486+STR, 274 pp., www.cesm.ucar.edu/models/cesm1.0/cam/docs/description/cam5_desc.pdf.

Neelin, J. D., O. Peters, and K. Hales, 2009: The transition to strong convection. *J. Atmos. Sci.*, **66**, 2367–2384, https://doi.org/10.1175/2009JAS2962.1.

Noori, R., F. Tian, R. Berndtsson, M. R. Abbasi, M. V. Naseh, A. Modabberi, A. Soltani, and B. Kløve, 2019: Recent and future trends in sea surface temperature across the Persian Gulf and Gulf of Oman. *PLOS ONE*, **14**, e0212790, https://doi.org/10.1371/journal.pone.0212790.

Numaguti, A., R. Oki, K. Nakamura, K. Tsuboki, N. Misawa, T. Asai, and Y.-M. Kodama, 1995: 4–5-day-period variation and low-level dry air observed in the equatorial western Pacific during the TOGA-COARE IOP. *J. Meteor. Soc. Japan*, **73**, 267–290, https://doi.org/10.2151/jmsj1965.73.2B_267.

Ogino, S.-Y., M. D. Yamanaka, S. Mori, and J. Matsumoto, 2016: How much is the precipitation amount over the tropical coastal region? *J. Climate*, **29**, 1231–1236, https://doi.org/10.1175/JCLI-D-15-0484.1.

O'Gorman, P. A., 2015: Precipitation extremes under climate change. *Curr. Climate Change Rep.*, **1**, 49–59, https://doi.org/10.1007/s40641-015-0009-3.

——, and T. Schneider, 2009: The physical basis for increases in precipitation extremes in simulations of 21st-century climate change. *J. Meteor. Soc. Japan*, **106**, 14 773–14 777, https://doi.org/10.2151/JMSJ1965.73.2B_267.

Pall, P., M. Allen, and D. A. Stone, 2007: Testing the Clausius–Clapeyron constraint on changes in extreme precipitation under CO_2 warming. *Climate Dyn.*, **28**, 351–363, https://doi.org/10.1007/s00382-006-0180-2.

Palmén, E., 1948: On the formation and structure of tropical hurricanes. *Geophysics*, 26–38.

Parsons, D. B., J.-L. Redelsperger, and K. Yoneyama, 2000: The evolution of the tropical western Pacific atmosphere–ocean system following the arrival of a dry intrusion. *Quart. J. Roy. Meteor. Soc.*, **126**, 517–548, https://doi.org/10.1002/qj.49712656307.

Pendergrass, A. G., and D. L. Hartmann, 2014: Changes in the distribution of rain frequency and intensity in response to global warming. *J. Climate*, **27**, 8372–8383, https://doi.org/10.1175/JCLI-D-14-00183.1.

Peters, O., and J. D. Neelin, 2006: Critical phenomena in atmospheric precipitation. *Nat. Phys.*, **2**, 393–396, https://doi.org/10.1038/nphys314.

Pfahl, S., P. A. O'Gorman, and E. M. Fischer, 2017: Understanding the regional pattern of projected future changes in extreme precipitation. *Nat. Climate Change*, **7**, 423–427, https://doi.org/10.1038/nclimate3287.

Powell, S. W., 2019: Observing possible thermodynamic controls on tropical marine rainfall in moist environments. *J. Atmos. Sci.*, **76**, 3737–3751, https://doi.org/10.1175/JAS-D-19-0144.1.

Qian, J.-H., 2008: Why precipitation is mostly concentrated over islands in the Maritime Continent. *J. Atmos. Sci.*, **65**, 1428–1441, https://doi.org/10.1175/2007JAS2422.1.

Raymond, D. J., 1995: Regulation of moist convection over the west Pacific warm pool. *J. Atmos. Sci.*, **52**, 3945–3959, https://doi.org/10.1175/1520-0469(1995)052<3945:ROMCOT>2.0.CO;2.

——, and M. M. Flores, 2016: Predicting convective rainfall over tropical oceans from environmental conditions. *J. Adv. Model. Earth Syst.*, **8**, 703–718, https://doi.org/10.1002/2015MS000595.

Rodwell, M. J., and B. J. Hoskins, 2001: Subtropical anticyclones and summer monsoons. *J. Climate*, **14**, 3192–3211, https://doi.org/10.1175/1520-0442(2001)014<3192:SAASM>2.0.CO;2.

Romps, D. M., 2010: A direct measure of entrainment. *J. Atmos. Sci.*, **67**, 1908–1927, https://doi.org/10.1175/2010JAS3371.1.

——, and Z. Kuang, 2010: Do undiluted convective plumes exist in the upper tropical troposphere? *J. Atmos. Sci.*, **67**, 468–484, https://doi.org/10.1175/2009JAS3184.1.

——, and A. B. Charn, 2015: Sticky thermals: Evidence for a dominant balance between buoyancy and drag in cloud updrafts. *J. Atmos. Sci.*, **72**, 2890–2901, https://doi.org/10.1175/JAS-D-15-0042.1.

Rushley, S., D. Kim, C. Bretherton, and M.-S. Ahn, 2018: Reexamining the nonlinear moisture–precipitation relationship over the tropical oceans. *Geophys. Res. Lett.*, **45**, 1133–1140, https://doi.org/10.1002/2017GL076296.

Schiro, K. A., and J. D. Neelin, 2019: Deep convective organization, moisture vertical structure, and convective transition using deep-inflow mixing. *J. Atmos. Sci.*, **76**, 965–987, https://doi.org/10.1175/JAS-D-18-0122.1.

——, ——, D. K. Adams, and B. R. Lintner, 2016: Deep convection and column water vapor over tropical land versus tropical ocean: A comparison between the Amazon and the tropical western Pacific. *J. Atmos. Sci.*, **73**, 4043–4063, https://doi.org/10.1175/JAS-D-16-0119.1.

——, F. Ahmed, S. E. Giangrande, and J. D. Neelin, 2018: GoAmazon2014/5 campaign points to deep-inflow approach to deep convection across scales. *Proc. Natl. Acad. Sci. USA*, **115**, 4577–4582, https://doi.org/10.1073/pnas.1719842115.

Schubert, W. H., and J. J. Hack, 1982: Inertial stability and tropical cyclone development. *J. Atmos. Sci.*, **39**, 1687–1697, https://doi.org/10.1175/1520-0469(1982)039<1687:ISATCD>2.0.CO;2.

Sherwood, S. C., 1999: Convective precursors and predictability in the tropical western Pacific. *Mon. Wea. Rev.*, **127**, 2977–2991, https://doi.org/10.1175/1520-0493(1999)127<2977:CPAPIT>2.0.CO;2.

——, D. Hernández-Deckers, M. Colin, and F. Robinson, 2013: Slippery thermals and the cumulus entrainment paradox. *J. Atmos. Sci.*, **70**, 2426–2442, https://doi.org/10.1175/JAS-D-12-0220.1.

Singh, M. S., and P. A. O'Gorman, 2013: Influence of entrainment on the thermal stratification in simulations of radiative-convective equilibrium. *Geophys. Res. Lett.*, **40**, 4398–4403, https://doi.org/10.1002/grl.50796.

Sobel, A. H., and C. S. Bretherton, 2000: Modeling tropical precipitation in a single column. *J. Climate*, **13**, 4378–4392, https://doi.org/10.1175/1520-0442(2000)013<4378:MTPIAS>2.0.CO;2.

——, J. Nilsson, and L. M. Polvani, 2001: The weak temperature gradient approximation and balanced tropical moisture waves. *J. Atmos. Sci.*, **58**, 3650–3665, https://doi.org/10.1175/1520-0469(2001)058<3650:TWTGAA>2.0.CO;2.

Stechmann, S. N., and J. D. Neelin, 2011: A stochastic model for the transition to strong convection. *J. Atmos. Sci.*, **68**, 2955–2970, https://doi.org/10.1175/JAS-D-11-028.1.

Stommel, H., 1947: Entrainment of air into a cumulus cloud. *J. Meteor.*, **4**, 91–94, https://doi.org/10.1175/1520-0469(1947)004<0091:EOAIAC>2.0.CO;2.

Sun, D., K. M. Lau, and M. Kafatos, 2008: Contrasting the 2007 and 2005 hurricane seasons: Evidence of possible impacts of Saharan dry air and dust on tropical cyclone activity in the Atlantic basin. *Geophys. Res. Lett.*, **35**, L15405, https://doi.org/10.1029/2008GL034529.

Sutton, R. T., B. Dong, and J. M. Gregory, 2007: Land/sea warming ratio in response to climate change: IPCC AR4 model results and comparison with observations. *Geophys. Res. Lett.*, **34**, L02701, https://doi.org/10.1029/2006GL028164.

Tokioka, T., K. Yamazaki, A. Kitoh, and T. Ose, 1988: The equatorial 30–60 day oscillation and the Arakawa–Schubert penetrative cumulus parameterization. *J. Meteor. Soc. Japan*, **66**, 883–901, https://doi.org/10.2151/jmsj1965.66.6_883.

Tuleya, R. E., 1994: Tropical storm development and decay: Sensitivity to surface boundary conditions. *Mon. Wea. Rev.*, **122**, 291–304, https://doi.org/10.1175/1520-0493(1994)122<0291:TSDADS>2.0.CO;2.

——, and Y. Kurihara, 1978: A numerical simulation of the landfall of tropical cyclones. *J. Atmos. Sci.*, **35**, 242–257, https://doi.org/10.1175/1520-0469(1978)035<0242:ANSOTL>2.0.CO;2.

Waite, M. L., and B. Khouider, 2010: The deepening of tropical convection by congestus preconditioning. *J. Atmos. Sci.*, **67**, 2601–2615, https://doi.org/10.1175/2010JAS3357.1.

Wang, C., D. B. Enfield, S. Lee, and C. W. Landsea, 2006: Influences of the Atlantic warm pool on Western Hemisphere summer rainfall and Atlantic hurricanes. *J. Climate*, **19**, 3011–3028, https://doi.org/10.1175/JCLI3770.1.

Wang, C.-C., B.-X. Lin, C.-T. Chen, and S.-H. Lo, 2014: Quantifying the effects of long-term climate change on tropical cyclone rainfall using a cloud-resolving model: Examples of two landfall typhoons in Taiwan. *J. Climate*, **28**, 66–85, https://doi.org/10.1175/JCLI-D-14-00044.1.

Wang, Z., M. T. Montgomery, and T. J. Dunkerton, 2010: Genesis of pre–Hurricane Felix (2007). Part I: The role of the easterly wave critical layer. *J. Atmos. Sci.*, **67**, 1711–1729, https://doi.org/10.1175/2009JAS3420.1.

Warner, J., 1955: The water content of cumuliform cloud. *Tellus*, **7**, 449–457, https://doi.org/10.3402/tellusa.v7i4.8917.

Willoughby, H. E., F. D. Marks, and R. J. Feinberg, 1984: Stationary and moving convective bands in hurricanes. *J. Atmos. Sci.*, **41**, 3189–3211, https://doi.org/10.1175/1520-0469(1984)041<3189:SAMCBI>2.0.CO;2.

Wu, P., M. Hara, J.-I. Hamada, M. D. Yamanaka, and F. Kimura, 2009: Why a large amount of rain falls over the sea in the vicinity of western Sumatra Island during nighttime. *J. Appl. Meteor. Climatol.*, **48**, 1345–1361, https://doi.org/10.1175/2009JAMC2052.1.

Yang, G.-Y., and J. Slingo, 2001: The diurnal cycle in the tropics. *Mon. Wea. Rev.*, **129**, 784–801, https://doi.org/10.1175/1520-0493(2001)129<0784:TDCITT>2.0.CO;2.

Yeo, K., and D. M. Romps, 2013: Measurement of convective entrainment using Lagrangian particles. *J. Atmos. Sci.*, **70**, 266–277, https://doi.org/10.1175/JAS-D-12-0144.1.

Yoneyama, K., 2003: Moisture variability over the tropical western Pacific Ocean. *J. Meteor. Soc. Japan*, **81**, 317–337, https://doi.org/10.2151/jmsj.81.317.

——, and D. B. Parsons, 1999: A proposed mechanism for the intrusion of dry air into the tropical western Pacific region. *J. Atmos. Sci.*, **56**, 1524–1546, https://doi.org/10.1175/1520-0469(1999)056<1524:APMFTI>2.0.CO;2.

Zavala-Hidalgo, J., A. Parés-Sierra, and J. Ochoa, 2002: Seasonal variability of the temperature and heat fluxes in the Gulf of Mexico. *Atmósfera*, **15**, 81–104.

Zhang, C., and J. Pennington, 2004: African dry air outbreaks. *J. Geophys. Res.*, **109**, D20108, https://doi.org/10.1029/2003JD003978.

Zhang, G. J., and N. A. McFarlane, 1995: Sensitivity of climate simulations to the parameterization of cumulus convection in the Canadian Climate Centre general circulation model. *Atmos.–Ocean*, **33**, 407–446, https://doi.org/10.1080/07055900.1995.9649539.

Zhu, Y., and R. E. Newell, 1998: A proposed algorithm for moisture fluxes from atmospheric rivers. *Mon. Wea. Rev.*, **126**, 725–735, https://doi.org/10.1175/1520-0493(1998)126<0725:APAFMF>2.0.CO;2.

Zipser, E. J., 2003: Some views on "hot towers" after 50 years of tropical field programs and two years of TRMM data. *Cloud Systems, Hurricanes, and the Tropical Rainfall Measuring Mission (TRMM)*, Meteor. Monogr., No. 51, Amer. Meteor. Soc., 49–58, https://doi.org/10.1175/0065-9401(2003)029<0049:CSVOHT>2.0.CO;2.

——, D. J. Cecil, C. Liu, S. W. Nesbitt, and D. P. Yorty, 2006: Where are the most intense thunderstorms on Earth? *Bull. Amer. Meteor. Soc.*, **87**, 1057–1072, https://doi.org/10.1175/BAMS-87-8-1057.

Zuidema, P., B. Mapes, J. Lin, C. Fairall, and G. Wick, 2006: The interaction of clouds and dry air in the eastern tropical Pacific. *J. Climate*, **19**, 4531–4544, https://doi.org/10.1175/JCLI3836.1.